JCB Journal of Cell Biology

ARTICLE

The amino acid transporter SLC-36.1 cooperates with PtdIns3P 5-kinase to control phagocytic lysosome reformation

Qiwen Gan[1,2], Xin Wang[1], Qian Zhang[2], Qiuyuan Yin[1], Youli Jian[2], Yubing Liu[3], Nan Xuan[2], Jinglin Li[1], Junxiang Zhou[2], Kai Liu[2], Yudong Jing[2], Xiaochen Wang[3], and Chonglin Yang[1]

Phagocytic removal of apoptotic cells involves formation, maturation, and digestion of cell corpse–containing phagosomes. The retrieval of lysosomal components following phagolysosomal digestion of cell corpses remains poorly understood. Here we reveal that the amino acid transporter SLC-36.1 is essential for lysosome reformation during cell corpse clearance in *Caenorhabditis elegans* embryos. Loss of *slc-36.1* leads to formation of phagolysosomal vacuoles arising from cell corpse–containing phagosomes. In the absence of *slc-36.1*, phagosome maturation is not affected, but the retrieval of lysosomal components is inhibited. Moreover, loss of PPK-3, the *C. elegans* homologue of the PtdIns3P 5-kinase PIKfyve, similarly causes accumulation of phagolysosomal vacuoles that are defective in phagocytic lysosome reformation. SLC-36.1 and PPK-3 function in the same genetic pathway, and they directly interact with one another. In addition, loss of *slc-36.1* and *ppk-3* causes strong defects in autophagic lysosome reformation in adult animals. Our findings thus suggest that the PPK-3–SLC-36.1 axis plays a central role in both phagocytic and autophagic lysosome formation.

Introduction

Lysosomes are major sites of cellular degradation, signal sensing, and signal transduction (Luzio et al., 2007; Settembre et al., 2013; Xu and Ren, 2015; Perera and Zoncu, 2016; Davidson and Vander Heiden, 2017). Dysfunction of lysosomes contributes to many human disorders including lysosome storage diseases and neurodegenerative disorders (Saftig and Klumperman, 2009; Ferguson, 2015). Lysosomes receive and degrade both intracellular and extracellular cargoes that are generated by autophagy, endocytosis, and phagocytosis (Luzio et al., 2007). These degradation activities quickly consume the pool of lysosomes in the cell. Thus, lysosomes need to regenerate following lysosomal degradation so as to maintain the homeostasis of the lysosome pool. To meet the demands of cellular degradation, the number of lysosomes can also be increased by activation of TFEB and TFE3, two transcription factors of lysosomal and autophagy genes (Settembre et al., 2011; Martina et al., 2014). TFEB and TFE3 promote transcription of lysosomal and autophagy genes by cytoplasm-to-nucleus translocation in mTOR-dependent or -independent manners (Li et al., 2016; Puertollano et al., 2018).

Recent studies have shed light on the mechanisms underlying lysosome reformation accompanying lysosomal degradation of autophagic and endocytic cargos. Lysosome reformation from autolysosomes, also referred to as autophagic lysosome reformation (ALR), involves phosphatidylinositol 4,5-bisphosphate–and clathrin-mediated membrane budding on autolysosomes, KIF5B-driven elongation of membrane tubules along microtubules, dynamin 2–dependent proto-lysosome scission, and finally proto-lysosome maturation (Chen and Yu, 2017, 2018). Spinster, a lysosomal sugar transporter, was also found to be essential for ALR in cells with prolonged starvation (Rong et al., 2011). Endocytic lysosome reformation is an ATP-dependent process, which also requires lysosomal acidification and intralysosomal Ca^{2+} (Pryor et al., 2000). In addition, the phosphatidylinositol 3-phosphate (PtdIns3P) 5-kinase PIKfyve and the lysosomal calcium channel TRPML1 are required for endocytic lysosome reformation (Nicot, 2006; Miller et al., 2015; Bissig et al., 2017). PIKfyve generates phosphatidylinositol 3,5-bisphosphate, which activates TRPML1 to control lysosomal Ca^{2+}

[1]State Key Laboratory of Conservation and Utilization of Bio-Resources in Yunnan, and Center for Life Sciences, School of Life Sciences, Yunnan University, Kunming, China; [2]State Key Laboratory of Molecular Developmental Biology, Institute of Genetics and Developmental Biology, Chinese Academy of Sciences, Beijing, China; [3]National Laboratory of Biomacromolecules, Chinese Academy of Sciences Center for Excellence in Biomacromolecules, Institute of Biophysics, Chinese Academy of Sciences, Beijing, China.

Correspondence to Chonglin Yang: clyang@ynu.edu.cn.

efflux (Dong et al., 2010; McCartney et al., 2014). Notably, PIKfyve, TRPML1, and mTOR were shown to regulate phagosome and entotic vacuole shrinkage (Krajcovic et al., 2013; Krishna et al., 2016), suggesting that these factors are important for lysosome regeneration on phagolysosomes. Nevertheless, the mechanisms underlying phagocytic lysosome reformation (PLR) remain mostly elusive.

Caenorhabditis elegans provides an excellent model for studying phagocytic clearance of apoptotic cells. In the lifetime of a *C. elegans* hermaphrodite, 131 somatic cells and about half the germ cells undergo apoptosis that is essentially controlled by a linear genetic pathway (Wang and Yang, 2016). The resulting cell corpses are recognized and phagocytosed by neighboring cells (Sulston and Horvitz, 1977; Sulston et al., 1983; Gumienny et al., 1999; Conradt et al., 2016). Two major signaling pathways, *ced-1/6/7* and *ced-2/5/12*, act redundantly to recognize and transduce engulfment signals to induce cytoskeleton reorganization of the engulfing cell, leading to cell corpse internalization and formation of membrane-bound phagosomes (Reddien and Horvitz, 2004). The cell corpse–enclosing phagosomes then undergo progressive acidification by sequentially interacting with early and late endosomes, and finally fuse with lysosomes to yield phagolysosomes (Flannagan et al., 2012; Wang and Yang, 2016). This process, termed phagosome maturation, involves multiple factors that are shared by endocytic trafficking and autophagy (Kinchen and Ravichandran, 2008). For example, small Rab GTPases and their effectors and regulators, including RAB-5, VPS-34, TBC-2, RAB-14, RAB-2, RAB-7, ARL-8, and the HOPS complex, act cooperatively to regulate phagosome maturation (Li et al., 2009; Xiao et al., 2009; Guo et al., 2010; Sasaki et al., 2013). Within the phagolysosomes, cell corpses are digested by lysosomal acidic hydrolases (Xu et al., 2014). However, an important question that remains unanswered is how lysosomes reform following phagolysosomal digestion of cell corpses.

In this study, we characterized PLR in the process of cell corpse clearance during *C. elegans* embryonic development. We reveal that SLC-36.1, which is homologous to the mammalian neutral amino acid transporters SLC36A1–4 (PAT1–4), functions as an essential regulator of PLR. We further demonstrate that PPK-3, the *C. elegans* PIKfyve homologue, is required for PLR and that SLC-36.1 and PPK-3 act together to promote PLR during embryonic development. In addition, we show that the SLC-36.1–PPK-3 axis is required for lysosome reformation from autolysosomes in adult animals. Thus, SLC-36.1 and PPK-3 not only are essential for PLR during embryonic cell corpse clearance but also serve as critical regulators in ALR in adult animals.

Results

Loss of *slc-36.1* leads to formation of embryonic cell corpse–derived vacuoles

To identify new factors that participate in phagocytic removal of apoptotic cells in *C. elegans*, we performed an ethyl methanesulfonate (EMS) mutagenesis screen to look for mutants that exhibit altered morphologies or numbers of embryonic cell corpses. By screening ∼12,000 haploid genomes, we identified a group of mutants that contained a number of vacuolar structures. These embryonic vacuoles, which are distinct from the conventional button-like apoptotic cell corpses, were rarely seen in WT (N2; Fig. 1 A). Seven of these mutants, *yq51*, *80*, *84*, *90*, *93*, *95*, and *110*, had comparable numbers of embryonic vacuoles and failed to complement one another (Fig. 1 B), indicating that they affected the same gene. We mapped these mutations to linkage group (LG) III and identified mutations in the *Y43F4B.7* gene, which encodes a putative membrane protein that shares sequence homology to the mammalian lysosomal neutral amino acid transporters SLC36A1–4 (Fig. 1 C; Sagné et al., 2001; Agulhon et al., 2003). *Y43F4B.7* was thus renamed *slc-36.1*. The *slc-36.1* mutants *yq51*, *80*, and *81* contained single nucleotide mutations that cause point mutations in the encoded protein, and the *yq80*, *90*, *95*, and *110* mutants had mutations in exon–intron splicing sites, leading to mis-splicing of the pre-mRNA and consequently to frame shifting of the ORF. Because the *yq110* mutation caused an early stop codon in the *slc-36.1* gene, it should be a strong loss-of-function allele of *slc-36.1*. Transgenic expression of WT *slc-36.1* driven by its own promoter strongly reduced the number of vacuoles in *slc-36.1(yq110)* embryos (Fig. 1 D), confirming that loss of *slc-36.1* was responsible for formation of the embryonic vacuoles.

To determine the identities of the embryonic vacuoles, we traced the development of WT and *slc-36.1(yq110)* embryos. In WT (N2) embryos, the button-like apoptotic cell corpses progressively shrank and disappeared within 30 min (27.6 ± 2.4 min; Fig. 1, E and F). In *slc-36.1(yq110)* embryos, while ∼18% of the button-like cell corpses condensed and disappeared as in WT, the majority of cell corpses did not shrink but instead exhibited a morphological switch from button-like to vacuoles (Fig. 1, E and F), indicating that these vacuoles were derived from apoptotic cell corpses. To consolidate this conclusion, we constructed double mutants of *slc-36.1(yq110)* with *egl-1(n3082)*, *ced-3(n717)*, and *ced-4(n1162)*, the strong loss-of-function mutations of the essential apoptosis genes *egl-1*, *ced-3*, and *ced-4* (Ellis and Horvitz, 1986; Conradt and Horvitz, 1998; Gumienny et al., 1999; Horvitz, 2003). Barely embryonic vacuoles were observed in these double mutants (Fig. 1 G). Thus, the vacuoles in *slc-36.1(yq110)* mutant embryos resulted from apoptotic cell corpses.

SLC-36.1 is a putative amino acid transporter that localizes to lysosomes

SLC-36.1 and its mammalian homologues SLC36A1–4 have similar topologies with 11 transmembrane domains (Fig. 2 A). *C. elegans* SLC-36.1, mammalian SLC36A1–4 and LYAAT-1, *Drosophila melanogaster* Path, and yeast AVT4 are members of the amino acid/auxin permease superfamily; they all contain a conserved iGsGif motif essential for the functions of amino acid transporters (Fig. 2 B; Bröer, 2014). Except for yeast AVT4, the other proteins are H^+-coupled amino acid transporters and contain a conserved histidine residue responsible for binding and translocating the protons required for transporter activity (Metzner et al., 2008). To determine if the amino acid transporter activity of SLC-36.1 is involved in formation of embryonic vacuoles, we expressed SLC-36.1 proteins with mutations in either the conserved histidine or the iGsGif motif. Compared with

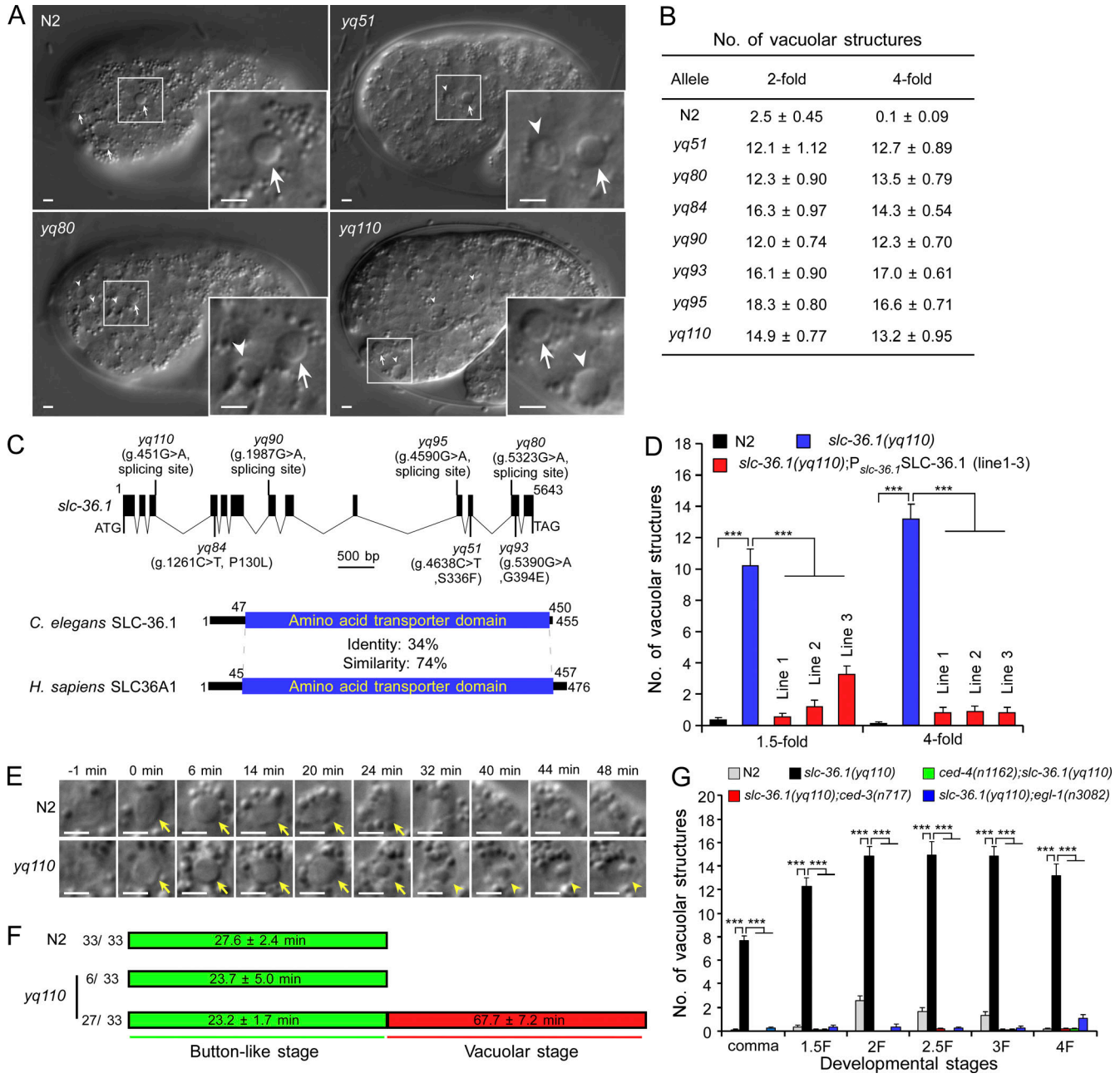

Allele	2-fold	4-fold
N2	2.5 ± 0.45	0.1 ± 0.09
yq51	12.1 ± 1.12	12.7 ± 0.89
yq80	12.3 ± 0.90	13.5 ± 0.79
yq84	16.3 ± 0.97	14.3 ± 0.54
yq90	12.0 ± 0.74	12.3 ± 0.70
yq93	16.1 ± 0.90	17.0 ± 0.61
yq95	18.3 ± 0.80	16.6 ± 0.71
yq110	14.9 ± 0.77	13.2 ± 0.95

Figure 1. ***slc-36.1* mutant embryos contain vacuoles arising from apoptotic cell corpses. (A)** DIC images of WT (N2), *yq51*, *yq80*, and *yq110* embryos. Arrows and arrowheads indicate button-like cell corpses and vacuoles, respectively. Boxed regions are magnified (2.5×) in insets. Bars, 2 µm. **(B)** Quantification (mean ± SEM) of vacuoles in 2-fold and 4-fold embryos in N2 and mutants. 15 embryos were scored at each stage for each strain. **(C)** Schematic representation of the *slc-36.1* gene and the encoded protein. Black boxes and thin lines indicate exons and introns, respectively. Mutation sites in all mutants are indicated. Blue boxes indicate amino acid transporter domain. **(D)** Quantification (mean ± SEM) of embryonic vacuoles in the indicated strains. 15 embryos at the 1.5-fold and 4-fold stages were scored for each strain. ***, P < 0.001. **(E and F)** Time-lapse recording of cell corpses in N2 and *slc-36.1(yq110)* embryos. Arrows and arrowheads indicate cell corpses and vacuoles, respectively (E). Bars, 2 µm. 33 cell corpses were examined for each strain. The duration of each stage (mean± SEM) is shown in F. **(G)** Quantification (mean ± SEM) of embryonic vacuoles in 1.5-fold and 4-fold embryos with the indicated genotypes. 15 embryos were scored at each stage (1.5F, 2F, 2.5F, 3F, and 4F represent 1.5-, 2-, 2.5-, 3-, and 4-fold, respectively) for each strain. ***, P < 0.001. *H. sapiens*, *Homo sapiens*.

the WT SLC-36.1 that fully rescued the vacuole phenotype in *slc-36.1(yq110)* embryos, mutant SLC-36.1 carrying mutations of the conserved residues (H57A, G66A, and L68S) or a deletion of iGsGif failed to completely rescue the abnormal embryonic vacuoles in *slc-36.1(yq110)* (Fig. 2 C). No rescuing activity was observed in *slc-36.1(yq110)* mutants expressing SLC-36.1 with a P130L mutation identified in *slc-36.1(yq84)* (Fig. 2 C). In contrast, mutation of Ser 69, which is not conserved in other transporters (Fig. 2 B), did not affect SLC-36.1 rescuing activity (Fig. 2 C). Thus, the amino acid transporter activity is important for SLC-36.1 to prevent the formation of embryonic vacuoles. To further understand the requirement for *slc-36.1* in embryonic

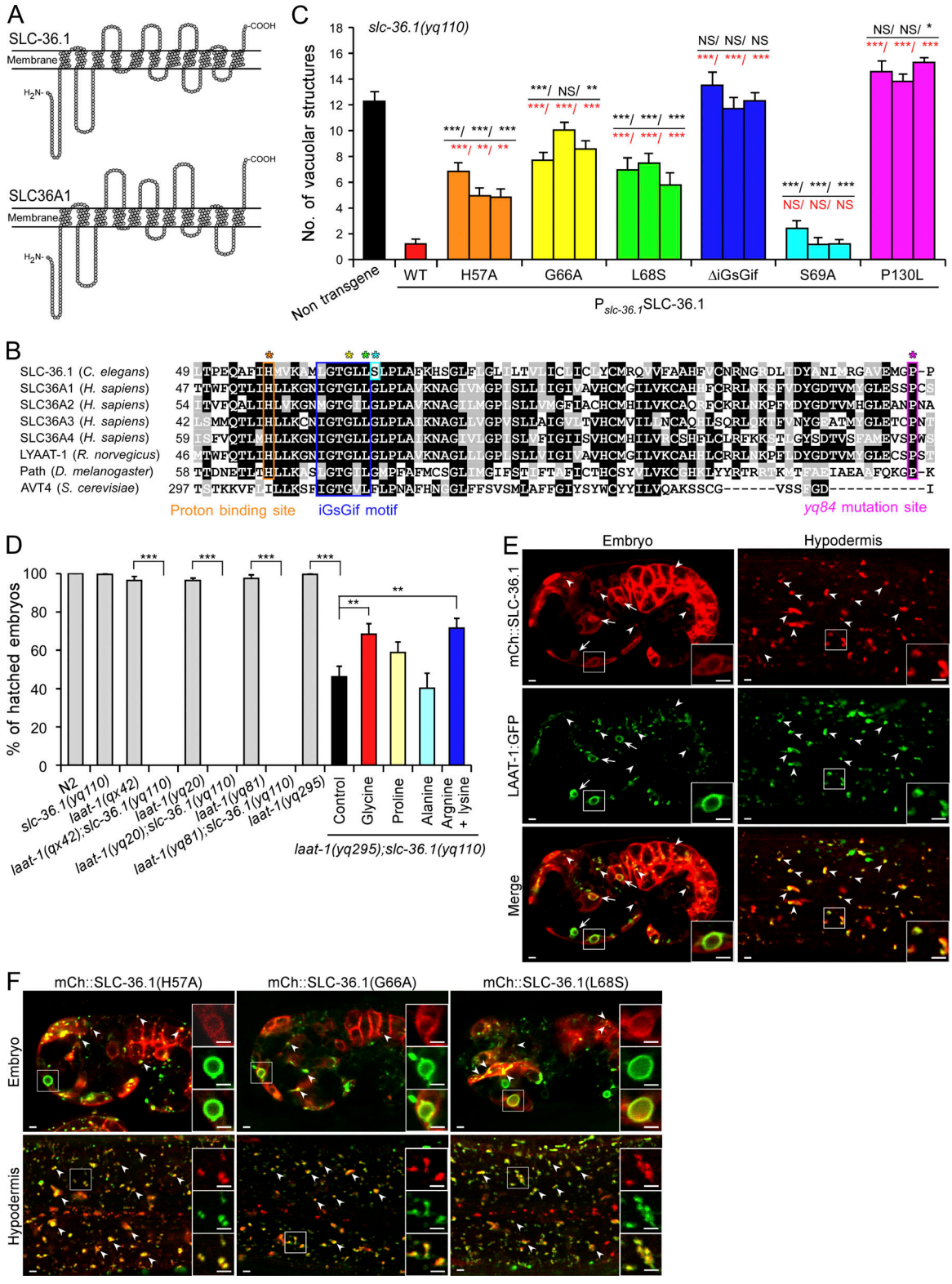

Figure 2. **SLC-36.1 is a putative lysosomal amino acid transporter. (A)** Topology models of *C. elegans* SLC-36.1 and *H. sapiens* SLC36A1. **(B)** Alignment of the amino acid transporter domains of *C. elegans* SLC-36.1, human SLC36A1-4, rat LYAAT-1, fly Path, and yeast AVT4. Identical residues are shaded in black, and similar ones in gray. The conserved H57, G66, and L68 are indicated in orange, yellow, and green, respectively. The blue star indicates the unconserved Ser 69. The mutation site in *slc-36(yq84)* mutants (P130L) is indicated in pink. **(C)** Quantification (mean ± SEM) of embryonic vacuoles in N2 and *slc-36.1(yq110)* and *slc-36.1(yq110)* mutants carrying the indicated transgenes. 15 embryos at the 1.5-fold stage were scored for each strain. Three independent transgenic lines were analyzed for each transgene. *, P < 0.05; **, P < 0.01; ***, P < 0.001. Black asterisks indicate comparisons between nontransgene and each SLC-36.1 transgenic line. Red asterisks indicate comparisons of transgenes between WT and mutant SLC-36.1 transgenic lines. **(D)** Quantification (mean ± SEM) of embryo lethality in N2, *slc-36.1* and *laat-1* single mutants and *laat-1;slc-36.1* double mutants without or with supplementation of amino acids. 250 or more embryos were

analyzed for each genotype. Indicated amino acids were supplied at 100 mM each, and data shown are derived from 10 independent experiments. Data are from three (non–amino acid supplementation group) or 10 (amino acid supplementation group) independent experiments. **, P < 0.01; ***, P < 0.001. **(E)** Colocalization of mCh::SLC-36.1 with LAAT-1::GFP in embryos (top) and adult hypodermis (bottom). Arrows and arrowheads indicate phagosomes and lysosomes, respectively. Boxed regions are magnified (2×) in insets. Bars, 2 µm. **(F)** Colocalization of mCh::SLC-36.1 carrying H57A, G66A, and or L68S mutations (red) with LAAT-1::GFP (green) in embryos (top) and adult hypodermis (bottom). Lysosomes are indicated by arrowheads. Insets show magnified (2×) views of boxed regions with mCh, GFP, and merged panels. Bars, 2 µm.

development, we examined the hatching ratio of *slc-36.1(yq110)* embryos and found that it was similar to WT (Fig. 2 D). Surprisingly, double mutants of *slc-36.1(yq110)* with *laat-1(qx42)* (Liu et al., 2012) or two additional *laat-1* mutants identified in this study, *yq20* and *yq81*, showed 100% embryonic lethality (Fig. 2 D). Consistent with this, double mutants of *slc-36.1(y110)* with the *laat-1(yq295)* weak loss-of-function mutant showed 54% embryonic lethality (Fig. 2 D). Supplementing the culture medium with glycine significantly ameliorated the embryonic lethality of *laat-1(yq295);slc-36.1(yq110)* double mutants, comparable to the rescuing effect by adding both lysine and arginine, the LAAT-1 substrates (Fig. 2 D). Given that LAAT-1 exports lysine and arginine out of the lysosome and its loss did not obviously affect embryonic survival (Liu et al., 2012), these findings suggest that *slc-36.1* likely acts as a neutral amino acid transporter that is required for embryonic development by coordinating with other lysosomal transporters to export amino acids from lysosomes.

We next investigated the expression and subcellular localization of SLC-36.1. Using the CRISPR/Cas9 assay, we knocked in the GFP-coding sequence right after the ATG initiation codon in the *slc-36.1* gene. Endogenous levels of GFP::SLC-36.1 were observed in embryos and multiple adult tissues, including the pharynx, intestine, hypodermis, and germ line, and the signal was enriched on the plasma membrane (Fig. S1 A). In the macrophage-like coelomocytes, GFP::SLC-36.1 localized to the membranes of lysosomes positive for the lysosomal DNase II NUC-1 (NUC-1::mCherry [mCh]; Fig. S1 B). Because the signal from GFP::SLC-36.1 was relatively weak, we further generated an mCh-fused SLC-36.1 (mCh::SLC-36.1) driven by the promoter of the engulfment cell-specific gene *ced-1*. In embryos, mCh::SLC-36.1 was found to localize to the plasma membrane and phagosomes that were positive for the lysosomal lysine/arginine transporter LAAT-1 fused with GFP (LAAT-1::GFP; Fig. 2 E). In the hypodermis, mCh::SLC-36.1 colocalized well with LAAT-1::GFP; Fig. 2 E). In addition, mCh::SLC-36.1 with H57A, G66A, or L68S mutations that reduced the rescuing activities of SLC-36.1 (Fig. 2 C) also colocalized with LAAT-1::GFP to phagosomes and lysosomes (Fig. 2 F). Altogether, these findings suggest that SLC-36.1 localizes and functions on lysosomes.

slc-36.1 acts at a late stage of phagocytic cell corpse clearance

Phagocytic removal of cell corpses requires their engulfment followed by delivery to lysosomes (Wang and Yang, 2016). To understand how SLC-36.1 plays a role in this process, we first examined whether cell corpse engulfment was defective in *slc-36.1(yq110)* embryos. In *C. elegans*, the *ced-1/6/7* and *ced-2/5/12* signaling pathways act redundantly to control cell corpse engulfment; thus, cell corpse engulfment is mostly blocked in *ced-1(e1735);ced-5(n1812)* double mutants (Reddien and Horvitz, 2004). In *ced-1(e1735);slc-36.1(yq110);ced-5(n1812)* triple mutants, the number of conventional button-like cell corpses remained similar to that in *ced-1(e1735);ced-5(n1812)* double mutants (Fig. 3 A); however, the number of embryonic vacuoles was greatly reduced compared with *slc-36.1(yq110)* single mutants (Fig. 3 B). This suggests that *slc-36.1* likely acts downstream of the engulfment genes. Consistent with this, the recruitment and release of the engulfment receptor CED-1::GFP to cell corpses in *slc-36.1(yq110)* was similar to that in WT (Fig. 3 C). However, the vacuoles in *slc-36.1(yq110)* embryos were negative for CED-1::GFP (Fig. 3 D and Fig. 4 F). Together, these data suggest that *slc-36.1* functions after CED-1 release from cell corpse–containing phagosomes (Chen et al., 2010).

We next investigated whether SLC-36.1 acts in phagosome maturation. We introduced into *slc-36.1(yq110)* mutants transgenic arrays expressing fluorescently tagged phagosome maturation factors, including YFP::2xFYVE, an indicator of phagosomal PtdIns3P; GFP::RAB-7, a small GTPase required for late endosome–phagosome fusion; LAAT-1::GFP, a lysosomal lysine/arginine transporter required for phagosomal digestion; NUC-1::mCh, a lysosomal DNase; and CPL-1::mChiOnt, a lysosomal cathepsin protease (Kinchen and Ravichandran, 2008; Guo et al., 2010; Liu et al., 2012; Xu et al., 2014). The button-like cell corpses in *slc-36.1(yq110)* embryos were positive for these phagosome maturation factors at a similar level to WT (Fig. 4, A–E), indicating that loss of *slc-36.1* did not affect phagosome maturation. However, the vacuoles were highly enriched for lysosomal components, including LAAT-1::GFP, NUC-1::mCh, and CPL-1::mChiOnt, but not phagosomal factors that act at earlier stages (Fig. 4, A–D and F). Thus, SLC-36.1 does not regulate phagosome maturation for phagolysosome formation, and the vacuoles in *slc-36.1* embryos were phagolysosomes. To consolidate this conclusion, we used high-voltage EM (HVEM) to examine the ultra-structures of cell corpses and vacuoles in both WT and *slc-36.1* embryos. WT cell corpses were more densely stained than living cells and could be classified into several groups, including unengulfed corpses (8.6%), corpses engulfed in early phagosomes (32.8%), and degrading phagolysosomes (50.0%; Fig. 4, G and H). Unlike the densely stained WT cell corpses, 66.3% of cell corpses in *slc-36.1(yq110)* embryos appeared as electron-lucent, and had few contents (Fig. 4, G and H). This suggests that phagolysosomes form in *slc-36.1(yq110)* embryos and have degradation capacities but fail to shrink. Using HIS-24::GFP, an apoptotic chromatin marker, and LAAT-1::mCh to monitor the dynamics of phagolysosomes, we found that HIS-24::GFP signals similarly disappeared following phagosomal recruitment of LAAT-1::mCh in both WT and *slc-36.1(yq110)* embryos (Fig. S2 A), suggesting that phagolysosomes are acidic in

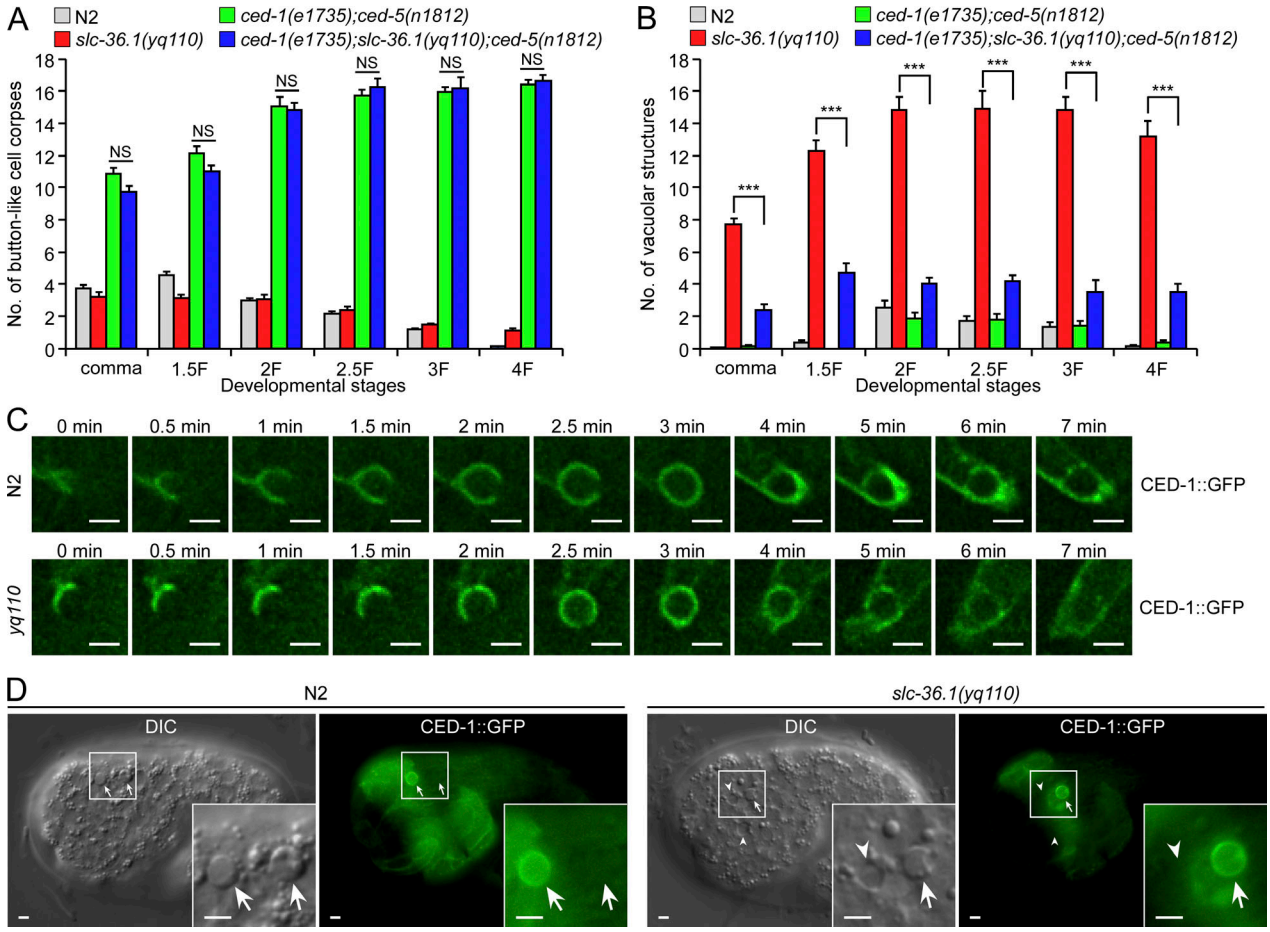

Figure 3. **Loss of *slc-36.1* does not affect engulfment of cell corpses. (A and B)** Quantification (mean ± SEM) of button-like cell corpses (A) and vacuoles (B) at different embryonic development stages in the indicated strains. 15 embryos were scored at each stage for each strain. ***, P < 0.001. **(C)** Time-lapse monitoring of CED-1::GFP kinetics on phagosomes in N2 and *slc-36.1(yq110)* embryos. The point when the CED-1::GFP ring was first detected on the cell corpse was set as 0 min. Bars, 2 µm. **(D)** Images of cell corpse labeling by CED-1::GFP in N2 and *slc-36.1(yq110)* embryos. Arrows and arrowheads indicate button-like cell corpses and vacuoles, respectively. Boxed regions are magnified (2×) in insets. Bars, 2 µm.

slc-36.1(yq110) mutants. In addition, *slc-36(yq110)* mutants, like WT, displayed normal lysosomal degradation of caveolin (GFP::CAV-1; Sato et al., 2006; Audhya et al., 2007), the low-density lipoprotein receptor RME-2 (RME-2::GFP; Grant and Hirsh, 1999), and the yolk protein VIT-2 (VIT-2::GFP; Grant and Hirsh, 1999) in early stage embryos. In contrast, these proteins accumulated in *laat-1(qx42)* loss-of-function mutants (Liu et al., 2012; Fig. S2, B–D). Altogether, these findings suggest that loss of *slc-36.1* does not affect lysosomal degradation but leads to formation of phagolysosomal vacuoles.

slc-36.1 is required for lysosome reformation from phagolysosomes

To understand how phagolysosomal vacuoles formed in *slc-36.1* embryos, we simultaneously monitored the dynamics of HIS-24::mCh and LAAT-1::GFP. In WT embryos, HIS-24::mCh–positive cell corpses first recruited LAAT-1::GFP–positive lysosomes to form phagolysosomes, which then progressively shrank and finally reached sizes similar to general lysosomes (Fig. 5, A and E; and Video 1). A more detailed time-lapse analysis indicated that, accompanying the shrinkage, phagolysosomes generated and released LAAT-1–positive tubules, forming new lysosomes that could be distinguished from the preexisting lysosomes (Fig. S3). This suggests that degradation of phagosomal contents occurred concomitantly with the retrieval of lysosomal components from the phagolysosome. In *slc-36.1(yq110)* embryos, HIS-24::mCh–positive phagosomes similarly recruited LAAT-1::GFP-marked lysosomes, confirming that phagolysosome formation was not defective (Fig. 5, A and C). However, the size of the phagolysosomes remained similar during the whole monitoring period (1 h), and barely any LAAT-1–positive tubules were generated on the phagolysosomes (Fig. 5, A, D and E; and Video 2). Thus, loss of *slc-36.1* does not affect phagosomal recruitment and fusion with lysosomes, but inhibits the retrieval of lysosomal contents from phagolysosomes. To test this further, we colabeled phagolysosomes with LAAT-1::GFP and NUC-1::mCh and performed time-lapse imaging. In WT, subsequent to incorporation of NUC-1::mCh into LAAT-1::GFP–positive phagolysosomes, both LAAT-1::GFP– and NUC-1::mCh–positive tubules were observed to bud from phagolysosomes concomitantly with the reduction of phagolysosome size (Fig. 5, B and E; and Video 3). In *slc-36.1(yq110)* mutants, however, barely any

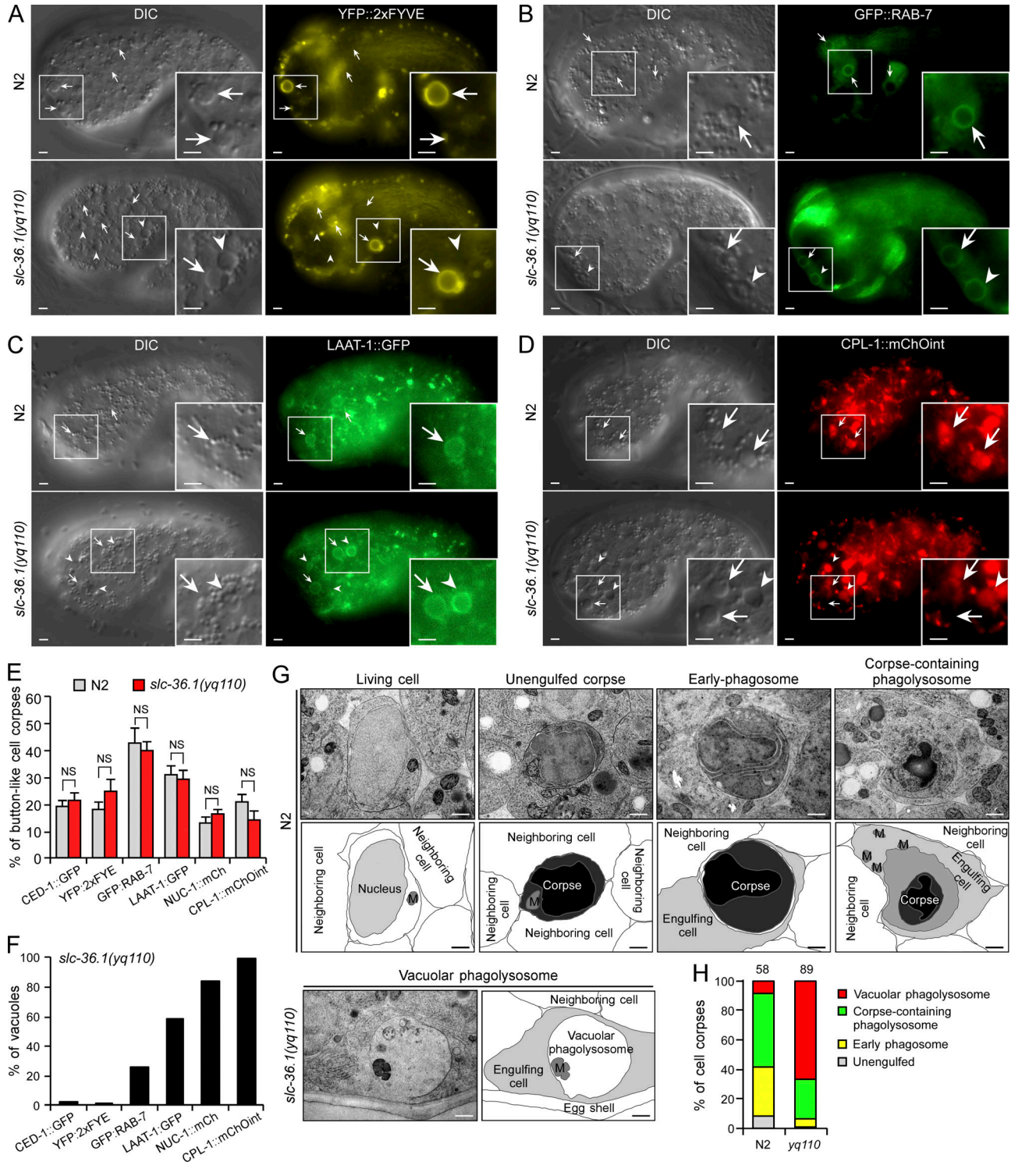

Figure 4. ***slc-36.1* functions after phagosome maturation. (A–D)** Images of cell corpse labeling by the phagosomal markers YFP::2xFYVE (A), GFP::RAB-7 (B), LAAT-1::GFP (C), and CPL-1::mChiOnt (D) in N2 and *slc-36.1(yq110)* embryos. Arrows and arrowheads indicate button-like cell corpses and vacuoles, respectively. Boxed regions are magnified (2×) in insets. Bars, 2 µm. **(E)** Quantification (mean ± SEM) of button-like cell corpses positive for phagosomal markers in N2 and *slc-36.1(yq110)* embryos. 15 embryos were scored at the 1.5-fold stage for each strain. Error bars represent SEM. **(F)** Quantification (mean ± SEM) of embryonic vacuoles positive for phagosomal markers in *slc-36.1(yq110)* embryos. 15 embryos were scored at the 1.5-fold stage for each strain. **(G)** HVEM images of a living cell and apoptotic cell corpses at the indicated phagosomal stages in N2 embryos (upper panels) and a phagolysosomal vacuole in a *slc-36.1(yq110)* embryo (lower panels). M, Mitochondria. Bars, 0.2 µm. **(H)** Quantification of cell corpses shown in G. The numbers of cell corpses analyzed for each genotype are indicated on the top of the columns.

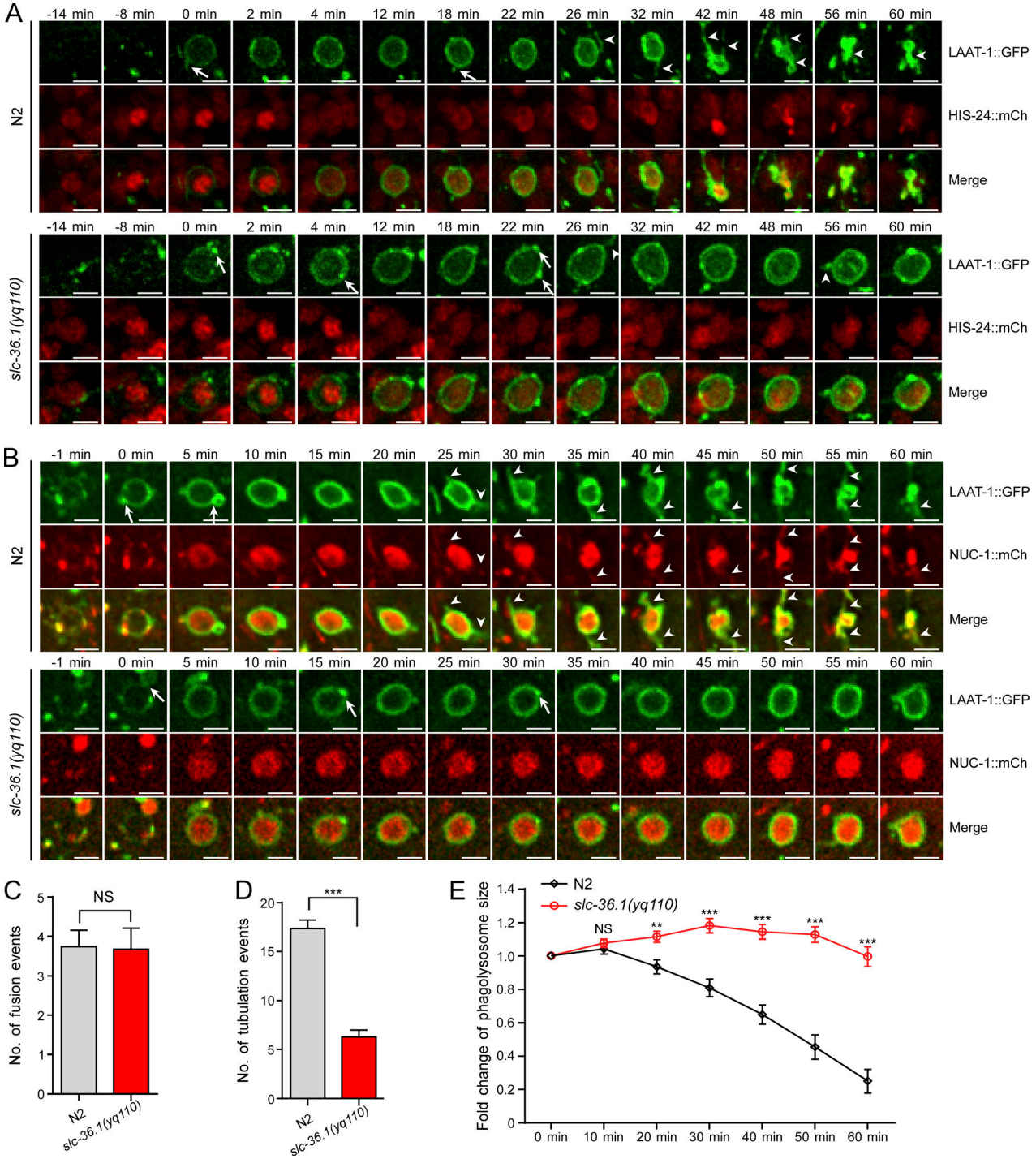

Figure 5. ***slc-36.1* is essential for PLR. (A)** Time-lapse chasing of LAAT-1::GFP– and HIS-24::mCh–positive phagolysosomes in N2 and *slc-36.1(yq110)* embryos. The time point that the LAAT-1::GFP ring was first detected on a cell corpses was set as 0 min. Arrows and arrowheads indicate lysosome fusion and lysosome tubulation, respectively. Bars, 2 µm. **(B)** Time-lapse chasing of LAAT-1::GFP– and NUC-1::mCh–positive phagolysosomes in N2 and *slc-36.1(yq110)* embryos. The time point that the LAAT-1::GFP ring was first detected on a cell corpse was set as 0 min. Arrows and arrowheads indicate lysosome fusion and lysosome tubulation, respectively. Bars, 2 µm. **(C–E)** Quantification (mean ± SEM) of lysosome fusion (C), tubulation (D), and change in phagolysosome sizes (E). 15 cell corpses were analyzed. **, P < 0.01; ***, P < 0.001.

such tubules were observed to form on phagolysosomes, while fusion of lysosomes with phagolysosomes still occurred (Fig. 5 B and Video 4). Together, these findings suggest that *slc-36.1* is required for reformation of lysosomes from phagolysosomes.

PPK-3/PIKfyve is required for PLR

Our genetic screen also identified *yq24* mutants that exhibited embryonic vacuoles similar to *slc-36.1* mutants (Fig. 6 A). Double mutants of *yq24* with *ced-4(n1162)* showed neither button-like

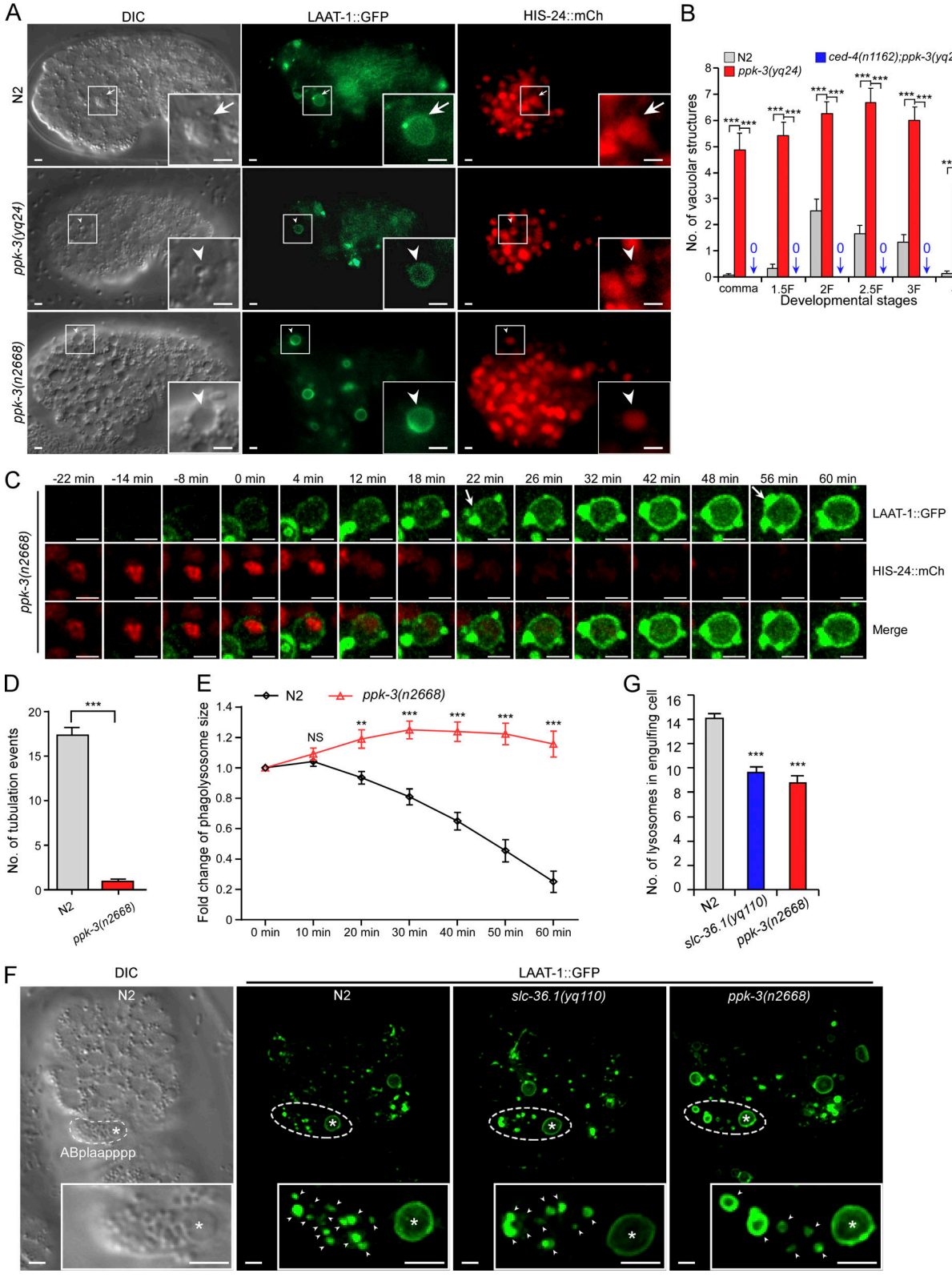

Figure 6. **PPK-3/PIKfyve is required for PLR. (A)** Images of LAAT-1::GFP– and HIS-24::mCh–positive embryonic cell corpses and vacuoles in N2, *ppk-3(yq24)*, and *ppk-3(n2668)* comma-stage embryos. Arrows and arrowheads indicate button-like cell corpses and vacuoles, respectively. Boxed regions are magnified (2.5×) in insets. Bars, 2 µm. **(B)** Time-course quantification of embryonic vacuoles in the indicated strains. 15 embryos were scored at each stage for each strain. ***, P < 0.001. **(C)** Time-lapse chasing of a LAAT-1::GFP– and HIS-24::mCh–positive cell corpse in a *ppk-3(n2668)* embryo. The time point that the LAAT-1::GFP ring was first detected on the cell corpse was set as 0 min. The arrow indicates lysosome fusion. Bars, 2 µm. **(D and E)** Quantification (mean ± SEM) of lysosome tubulation (D) and change in phagolysosome sizes (E). 15 cell corpses were analyzed. **, P < 0.01; ***, P < 0.001. **(F)** DIC image of an N2 comma-stage embryo showing the cell corpse-engulfing ABplaapppp cell and fluorescent images of N2, *slc-36.1(yq110)*, and *ppk-3(n2668)* comma-stage embryos expressing

LAAT-1::GFP. ABplaapppp cells are indicated by dotted circles and magnified (2.4×) in insets. Asterisks and arrowheads indicate phagolysosomes and lysosomes, respectively. Bars, 2 µm. **(G)** Quantification (mean ± SEM) of lysosomes in ABplaapppp cells. 40 or more ABplaapppp cells in each genotype were analyzed. ***, P < 0.001.

apoptotic cell corpses nor vacuolar structures (Fig. 6 B). The *yq24* embryonic vacuoles were enriched for both LAAT-1::GFP and HIS-24::mCh (Fig. 6 A). These data suggest that *yq24* embryonic vacuoles were phagolysosomes arising from apoptosis. Further genetic analysis revealed that *yq24* mutants carried an S1448L mutation in PPK-3, the *C. elegans* homologue of mammalian PtdIns3P 5-kinase PIKfyve. We thus examined *ppk-3(n2668)* strong loss-of-function mutants (Nicot, 2006). *ppk-3(n2668)* embryos contained many vacuolar structures of different sizes, a subset of which were positive for both LAAT-1::GFP and HIS-24::mCh (Fig. 6 A), indicating that they were phagolysosomes. Using time-lapse imaging, we found that HIS-24::mCh–positive cell corpses recruited LAAT-1::GFP–positive lysosomes to form phagolysosomes in *ppk-3(n2668)* embryos, similar to WT (Fig. 5 A, Fig. 6 C, and Video 5). However, no tubules were observed to form on the phagolysosomes, which failed to condense and remained similar in size during the whole monitoring period (Fig. 6, C–E). In addition, we observed that LAAT-1::GFP–positive lysosomes kept being recruited to the phagolysosomes (Fig. 6 C). These findings suggest that PPK-3, like SLC-36.1, is required for lysosome retrieval/reformation from phagolysosomes. In addition, we examined the amount of lysosomes in the cell corpse–engulfing ABplaapppp cells (Li et al., 2013). LAAT-1::GFP–positive lysosomes were significantly reduced in ABplaapppp cells in *slc-36.1(yq110)* and *ppk-3(n2668)* embryos compared with those in WT (Fig. 6, F and G), suggesting PLR is important for maintenance of the regular number of lysosomes within engulfing cells.

SLC-36.1 acts together with PPK-3

We next investigated whether SLC-36.1 and PPK-3 act together to control PLR. *ppk-3(n2668)* embryos had a higher number of HIS-24::mCh–positive vacuoles than *slc-36.1(yq110)* embryos; however, double mutants of *slc-36.1(yq110)* with *ppk-3(n2668)* exhibited a similar number of HIS-24::mCh–positive vacuoles to *ppk-3(n2668)* single mutants (Fig. 7, A and B). Using time-lapse imaging, we monitored phagolysosome condensation and lysosomal reformation in *slc-36.1(yq110);ppk-3(n2668)* double mutants. Phagolysosomes in *slc-36.1(yq110);ppk-3(n2668)* embryos showed similar kinetics of size reduction to *ppk-3(n2668)* single mutants (Fig. 7 C). Consistent with this, the lysosome reformation defect was not further enhanced in *slc-36.1(yq110);ppk-3(n2668)* double mutants compared with *ppk-3(n2668)* single mutants (Fig. 7 D). These data suggest that *slc-36.1* and *ppk-3* function in the same genetic pathway to control lysosome reformation.

We next examined the localization of PPK-3 and SLC-36.1 and found that GFP::PPK-3 and mCh::SLC-36.1 colocalized to phagosomes (Fig. 7 E). Using the microscale thermophoresis (MST) assay, we further found that EGFP::SLC-36.1 and Myc–His–PPK-3 form a complex (Fig. 7 F). To investigate if they interact directly, we generated and purified GST–SLC-36.1(1–53) and GST–SLC-36.1(101–142), which contain the cytosolic N terminus and loop 2 of SLC-36.1, respectively (Fig. 7 G). In GST pull-down assays, GST–SLC-36.1(101–142) directly interacted with ^{35}S-labeled PPK-3(1–668) and PPK-3(669–1497) (Fig. 7 G), suggesting that SLC-36.1 and PPK-3 interact at multiple sites. Altogether, these findings suggest that SLC-36.1 acts together with PPK-3 to control PLR.

The SLC-36.1–PPK-3 axis is essential for ALR

Finally, we investigated whether the SLC-36.1–PPK-3 axis also plays an essential role in ALR in adult animals, in which no cell death occurs. Interestingly, *slc-36.1(yq110)* adult animals displayed enlarged vacuolar structures that were positive for LAAT-1::GFP, NUC-1::mCh, and GFP::LGG-2 in the hypodermis, which were rarely seen in the WT (Fig. 8 A and Fig. S4). This suggests that the enlarged vacuoles in *slc-36.1(yq110)* hypodermis were likely autolysosomes. The autophagosome formation defective *atg-2(bp576)* mutants (Lu et al., 2011) showed no obvious enlargement of LAAT-1::GFP– and NUC-1::mCh-lysosomes (Fig. 8 A). In double mutants of *slc-36.1(yq110)* with *atg-2(bp576)*, the enlarged LAAT-1::GFP– and NUC-1::mCh–positive vacuoles were restored to *atg-2(bp576)* levels (Fig. 8, A and E). Importantly, starvation greatly increased the sizes of hypodermal vacuoles in *slc-36.1(yq110)*, but this change was suppressed by *atg-2(bp576)* (Fig. 8, B and E). RNAi of *lgg-1* or *lgg-2*, the *C. elegans* homologues of Atg8/LC3, similarly suppressed starvation-induced enlargement of NUC-1::mCh–positive lysosomes in *slc-36.1(yq110)* hypodermis (Fig. 8 C). Together, these findings suggest that loss of *slc-36.1* caused accumulation of enlarged autolysosomes in the hypodermis. Like *slc-36.1* mutants, *ppk-3(yq24)* mutants displayed enlargement of LAAT-1::GFP– and NUC-1::mCh–positive vacuoles in the hypodermis following starvation treatment, and this change was suppressed by *atg-2(bp576)* or RNAi of *lgg-1* or *lgg-2* (Fig. 8, D–F). With normal feeding, the *ppk-3(n2668)* strong loss-of-function mutants accumulated numerous enlarged NUC-1–positive autolysosomes, similar to starvation-treated *ppk-3(yq24)* mutants (Fig. 8, D, F, and G). Importantly, the double mutants of *slc-36.1(yq110)* with *ppk-3(n2668)* contained enlarged autolysosomes similar to *ppk-3(n2668)* single mutants (Fig. 8, G and H), suggesting that *slc-36.1* acts with *ppk-3* to regulate autolysosomes. To determine if *slc-36.1* and *ppk-3* are required for ALR, we compared the dynamics of NUC-1::mCh lysosomes in hypodermal cells in WT with NUC-1::mCh vacuoles in *slc-36.1* and *ppk-3* mutant hypodermal cells. In the WT, NUC-1::mCh tubules frequently extended from lysosomes (Fig. 8 I and Video 6). In contrast, no tubules were found to extend from the enlarged autolysosomes in *slc-36.1(yq110)* and *ppk-3(n2668)* mutants (Fig. 8 I and Videos 7 and 8). These data suggest that *slc-36.1* and *ppk-3* are essential for ALR. To consolidate this point, we examined lysosomes in the hypodermis using HVEM. In WT, the majority of lysosomes (84.6%) are electron dense with an average area of 0.48 µm^2 (Fig. 9, A and D). Remarkably, around 10% of lysosomes were observed to extend electron-lucent tubules (Fig. 9, B

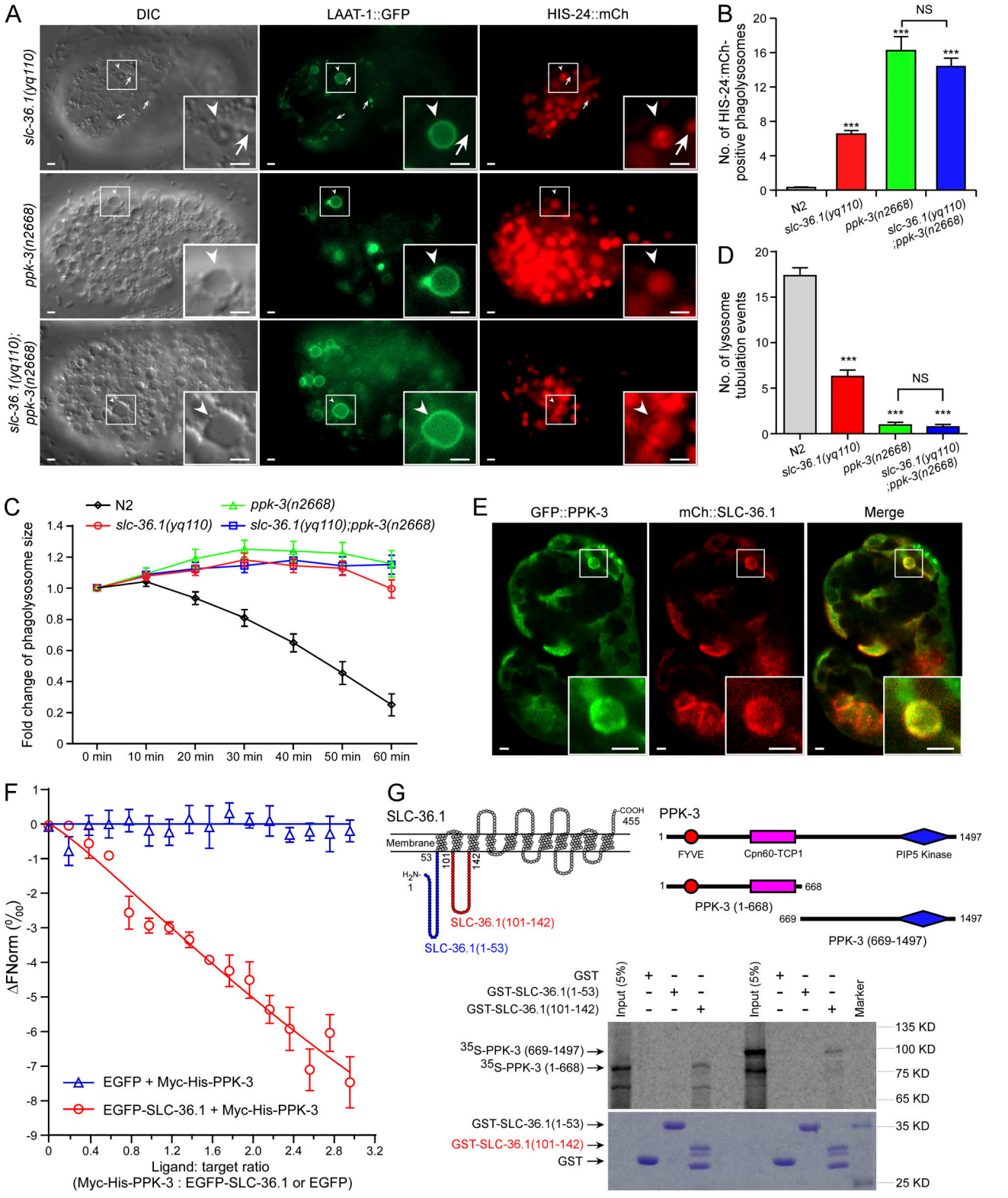

Figure 7. **SLC-36.1 functions together with PPK-3 in PLR. (A)** Images of LAAT-1::GFP– and HIS-24::mCh–positive cell corpses and phagolysosomal vacuoles in *slc-36.1(yq110)* and *ppk-3(n2668)* single mutants and *slc-36.1(yq110);ppk-3(n2668)* double mutants. Arrows and arrowheads indicate cell corpses and phagolysosomal vacuoles, respectively. Boxed regions are magnified (2.5×) in insets. Bars, 2 µm. **(B)** Quantification (mean ± SEM) of the sizes of HIS-24::mCh–positive vacuoles. 15 embryos were scored at the comma stage for each strain. ***, P < 0.001. **(C and D)** Quantification (mean ± SEM) of the change in phagolysosome sizes (C) and lysosome tubulation events (D). 15 cell corpses were quantified for each strain. ***, P < 0.001. **(E)** Colocalization of GFP::PPK-3 and mCh::SLC-36.1 to phagosomes in an N2 embryo. Boxed regions are magnified (2.5×) in insets. Bars, 2 µm. **(F)** Binding curve of Myc–His–PPK-3 to EGFP::SLC-36.1 measured by MST. EGFP was used as the negative control. ΔFnorm, normalized fluorescence ratio of initial fluorescence to fluorescence after laser heating. **(G)** Purified GST–SLC-36.1(1–53) or GST–SLC-36.1(101–142) was incubated with ^{35}S-labeled PPK-3(1–668 or 669–1497) and pulled down with glutathione-Sepharose beads. Precipitated proteins were resolved by SDS-PAGE and viewed with autoradiography.

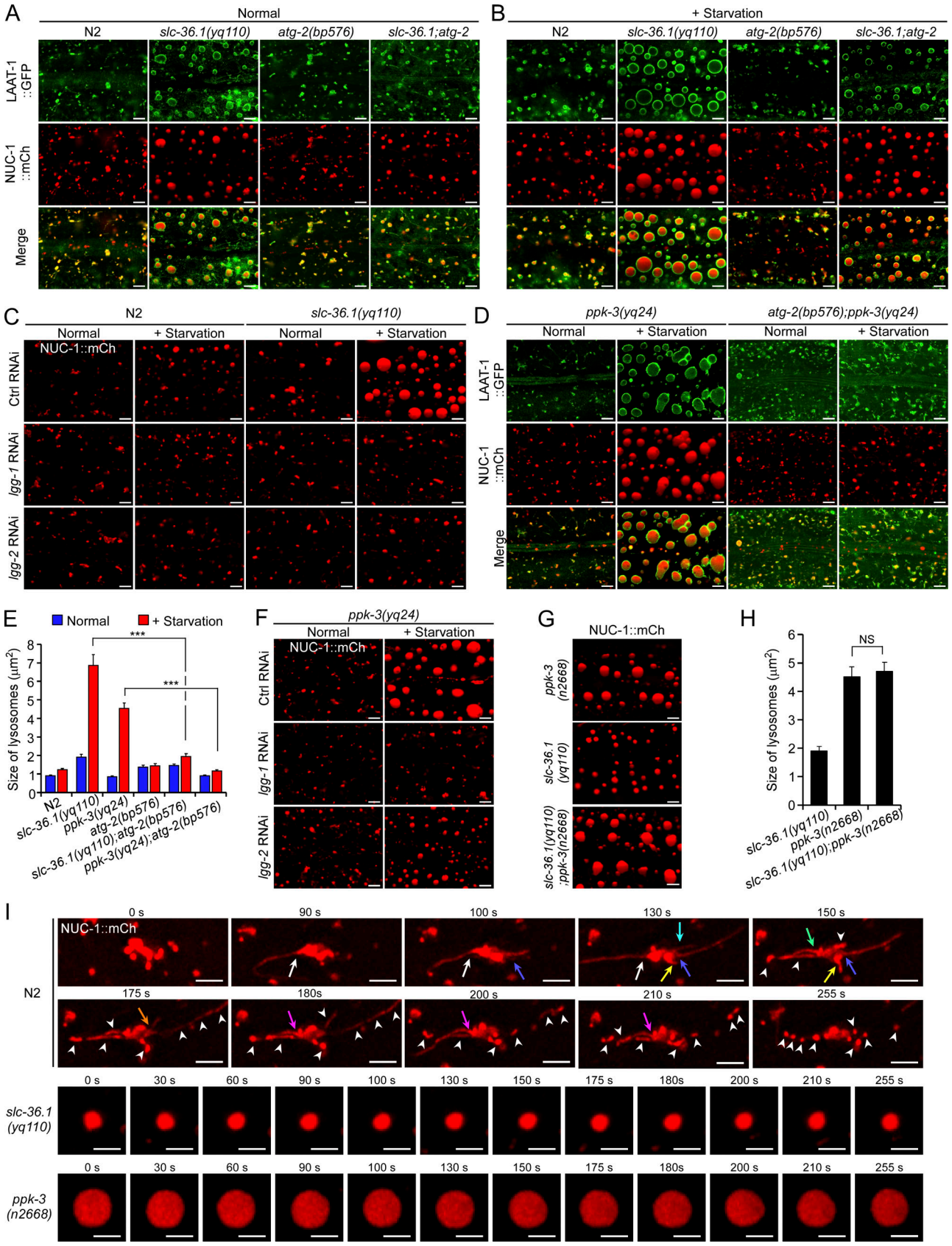

Figure 8. **The SLC-36.1–PPK-3 axis is required for ALR. (A and B)** Images of LAAT-1::GFP– and NUC-1::mCh–positive vacuoles in the posterior hypodermis in adult animals of the indicated genotypes without (A) or with starvation (B). Bars, 5 µm. **(C)** Images of NUC-1::mCh–positive hypodermal vacuoles in N2 and *slc-36.1(yq110)* adults treated with control (Ctrl) or *lgg-1* or *lgg-2* RNAi under normal and starvation conditions. Bars, 5 µm. **(D)** Images of LAAT-1::GFP– and

NUC-1::mCh–positive vacuoles in the posterior hypodermis in *ppk-3(yq24)* and *atg-2(bp576);ppk-3(yq24)* adult animals without or with starvation. Bars, 5 µm. **(E)** Quantification (mean ± SEM) of the sizes of NUC-1::mCh–positive lysosomes in the posterior hypodermis of adult animals with the indicated genotypes without or with starvation. ***, P < 0.001. **(F)** Images of NUC-1::mCh–positive hypodermal vacuoles in *ppk-3(yq24)* adult animals treated with control (Ctrl) or *lgg-1* or *lgg-2* RNAi under normal and starvation conditions. Bars, 5 µm. **(G)** Images of NUC-1::mCh–positive hypodermal vacuoles in *ppk-3(n2668)*, *slc-36.1(yq110)*, and *slc-36.1(yq110);ppk-3(n2668)* adult animals. Bars, 5 µm. **(H)** Quantification (mean ± SEM) of the sizes of NUC-1::mCh–positive hypodermal vacuoles as shown in G. ***, P < 0.001. **(I)** Time-lapse chasing of lysosome tubulation on autolysosomes in the hypodermis of N2, *slc-36.1(yq110)*, and *ppk-3(n2668)* adults. Lysosomal tubulation events are indicated with arrows of different colors. White arrowheads indicate newly formed lysosomes. Bars, 5 µm.

and E). In general, formation of these tubules appeared to involve polarization, tubulation, extension, and scission (Fig. 9 B). These electron-lucent lysosomal tubules are consistent with those observed with fluorescent microscopy (Fig. 8 I). In *slc-36.1(yq110)* and *ppk-3(yq24)* mutant hypodermis, however, the average area of lysosomes was greatly increased (average area of 0.89 and 0.69 µm^2, respectively; Fig. 9, C and D). Moreover, 43.4% and 49.4% of these enlarged lysosomes were electron-lucent, and lysosomal tubules were barely observed (Fig. 9 E). In *ppk-3(n2668)* strong loss-of-function mutants, hypodermal lysosomes were even larger than in *ppk-3(yq24)* and *slc-36.1(yq110)* mutants, which were mostly electron-lucent with no lysosomal tubules (Fig. 9, C–E). Altogether, these findings further suggest that the SLC-36.1–PPK-3 axis is required for ALR in adult animals.

Discussion

Although the regulators and mechanisms controlling cell corpse engulfment and phagosome maturation have been mostly revealed, little is known about the retrieval of lysosomal contents, i.e., lysosome reformation, the terminal step of cell corpse clearance. In this study, we characterized PLR during *C. elegans* embryonic development. We revealed that the lysosomal amino acid transporter SLC-36.1 and the PtdIns3P 5-kinase PPK-3 are essential regulators of lysosome reformation following phagolysosomal digestion of cell corpses. Our results indicated that loss of *slc-36.1* did not impair cell corpse engulfment and the subsequent phagosome maturation process; instead, it strongly delayed the reformation of lysosomes from phagolysosomes. Failure of lysosome reformation blocked the shrinkage of cell corpse–degrading phagolysosomes, resulting in formation of vacuoles in embryos. At the same time, our genetic screen also identified *ppk-3* mutants that show similar embryonic vacuoles to *slc-36.1* mutants. We further found that loss of *ppk-3* function, like *slc-36.1*, abrogated lysosome reformation from phagolysosomes. Double mutants of *slc-36.1* with *ppk-3* did not show an enhanced embryonic vacuole phenotype compared with single *ppk-3* strong loss-of-function mutants, which suggests that *slc-36.1* and *ppk-3* function in the same genetic pathway. In addition, SLC-36.1 and PPK-3 colocalize to phagosomes, and they physically interact with one another. These facts suggest that SLC-36.1 and PPK-3 act together to control PLR in the process of apoptotic cell removal during embryonic development in *C. elegans*.

Our findings revealed that, in adult hypodermis where no cell death occurs, SLC-36.1 and PPK-3 play an essential role in ALR. Under normal feeding conditions, *slc-36.1* strong loss-of-function mutants show enlarged lysosomes in the hypodermis. With starvation, the abnormal lysosomal enlargement was greatly enhanced. The enlargement of lysosomes in normally fed or starved animals was inhibited by loss of *atg-2* and RNAi of *lgg-1* or *lgg-2*, indicating that the enlarged lysosomes are autolysosomes generated by autophagy. Using live-cell imaging and HVEM, we found that no lysosomal tubulation occurred on the enlarged autolysosomes in *slc-36.1* and *ppk-3* hypodermis, which contrasts with the frequent budding and tubulation of lysosomes in WT. Our genetic data suggest that, like embryonic PLR, adult ALR requires the SLC-36.1–PPK-3 axis. In addition, given that PPK-3 was found to regulate terminal lysosome maturation (Bissig et al., 2017), it is likely that the SLC-36.1–PPK-3 axis also plays a pivotal role in lysosome reformation from endolysosomes.

In mammalian cells, the PtdIns3P 5-kinase PIKfyve regulates vacuole shrinkage and cargo redistribution during engulfment, which is achieved in part through the PIKfyve effector TRPML1 (Nicot, 2006; Krishna et al., 2016; Bissig et al., 2017). PIKfyve promotes the export of amino acids and other nutrients from vacuoles concomitantly with vacuole shrinkage to support the growth of engulfing cells during starvation (Krishna et al., 2016). In addition, TRPML1 was found to be required for the scission of lysosomes during lysosome reformation from endolysosomes (Miller et al., 2015). However, neither PIKfyve nor TRPML1 is a lysosomal nutrient transporter that executes the function of nutrient export from vacuoles/lysosomes. Our study now establishes SLC-36.1 as an essential regulator of phagocytic and ALR, which suggests that SLC-36.1 is likely responsible for export of amino acids, e.g., neutral amino acids, from phagolysosomes and autolysosomes. Failure to export amino acids likely prevents lysosome reformation from phagolysosomes and autolysosomes. Remarkably, export of amino acids from phagolysosomes and autolysosomes is essential for the development of embryos, as evidenced by the fact that double mutants of *slc-36.1* with *laat-1* display high penetrance of embryonic lethality, though *slc-36.1* and *laat-1* single mutant embryos develop fairly well (Fig. 2 D). These findings suggest that the function of PPK-3/PIKfyve in the regulation of cargo redistribution is likely achieved through amino acid transporters. Because mutations affecting SLC-36.1 transporter activity strongly reduced its rescuing effect on the defective phagolysosome shrinkage (Fig. 2 D), it is likely that amino acid pumping is coupled to PIKfyve-dependent lysosomal tubulation, which ensures that lysosomal shrinkage coincides with export of amino acids. It remains to be determined whether PPK-3/PIKfyve acts through phosphatidylinositol 3,5-bisphosphate to promote the activities of SLC-36.1 and other amino acid transporters, such as LAAT-1. In addition, given that PIKfyve and PAT1 and PAT4, two mammalian homologues of SLC-36.1, have been found to be important for mTOR activation (Heublein et al., 2010; Zheng et al., 2016; Shang et al., 2017), it is reasonable to hypothesize that the

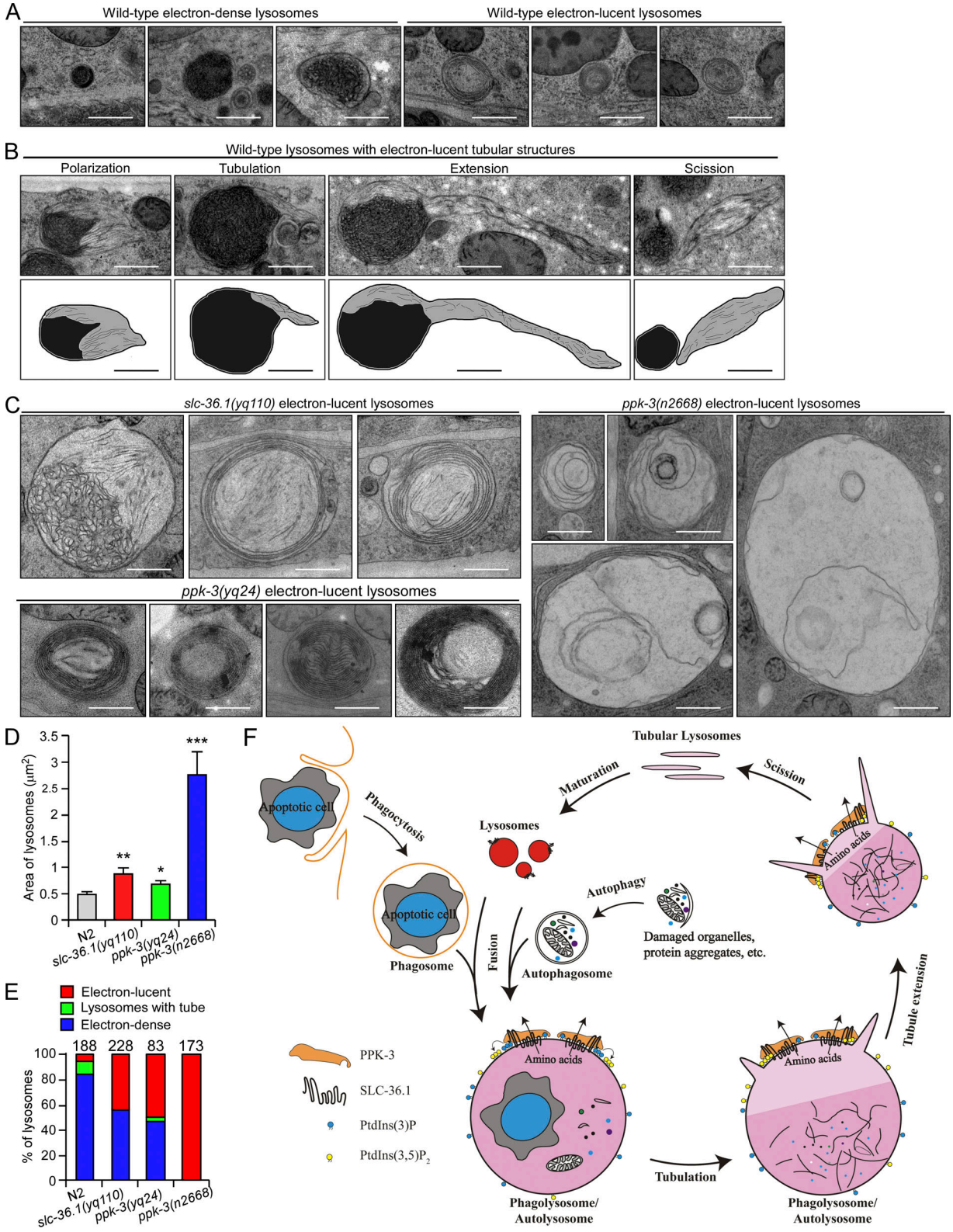

Figure 9. **HVEM examination of lysosomes in the hypodermis of N2, *slc-36.1(yq110)*, and *ppk-3(yq24)* adult animals.** Membrane-bound spherical organelles filled with membrane debris were identified as lysosomes. **(A)** HVEM images of electron-dense and electron-lucent lysosomes in the hypodermis of N2 animals. Bars, 0.5 µm. **(B)** HVEM images (top) of lysosomes undergoing different steps of lysosomal reformation in N2 hypodermis. Traces of lysosome reformation at each step are shown underneath. Bars, 0.5 µm. **(C)** HVEM images of electron-lucent lysosomes in the hypodermis of *slc-36.1(yq110)*, *ppk-3(yq24)*, and *ppk-3(n2668)* animals. Bars, 0.5 µm. **(D)** Quantification (mean ± SEM) of lysosome sizes in N2, *slc-36.1(yq110)*, *ppk-3(yq24)*, and *ppk-3(n2668)* adult hypodermis. 50 lysosomes were measured for each genotype. *, P < 0.05; **, P < 0.01; ***, P < 0.001. **(E)** Percentage of lysosomes with different morphologies shown in A–C in N2, *slc-36.1(yq110)*, *ppk-3(yq24)*, and *ppk-3(n2668)* adult hypodermis. For each genotype, indicated number of lysosomes from ≥10 electron microscopic sections of two or three worms were analyzed. **(F)** Graphic summary of the SLC-36.1–PPK-3 axis in lysosome reformation from phagolysosomes and autolysosomes.

SLC-36.1–PPK-3/PIKfyve axis plays a pivotal role in mTOR activation in the process of phagocytic clearance of apoptotic cell corpses as well as autophagy, similar to the requirement for the sugar transporter spinster (Rong et al., 2011). PPK-3/PIKfyve may also activate SLC-36.1 through physical interaction, as is the case for PIKfyve regulation of several membrane transporters, such as the Ca^{2+} channel TRPV6 (Sopjani et al., 2010), the glucose cotransporter SLC5A1 (Shojaiefard et al., 2007), the neutral amino acid transporter SLC6A19 (Bogatikov et al., 2012), and the glutamate transporters EAAT2, EAAT3, and EAAT4 (Gehring et al., 2009; Klaus et al., 2009; Alesutan et al., 2010). Our findings also suggest that, in addition to SLC-36.1, other amino acid transporters (e.g., LAAT-1/PQLC2), may be regulated by PIKfyve to promote lysosomal export of degradation products, which facilitates lysosome reformation from phagolysosomes and autolysosomes as well as endolysosomes.

Materials and methods

C. elegans strains

The N2 Bristol strain was used as the WT. *slc-36.1* mutants (*yq51*, *80*, *84*, *90*, *93*, *95*, and *110*), *laat-1* mutants (*yq20*, *81*, and *295*), and *ppk-3(yq24)* mutants were isolated by EMS mutagenesis. Other mutant alleles used in this study are listed by LGs: LG I *ced-1(e1735)*; LG II, *laat-1(qx42)*; LG III, *ced-4(n1162)*; LG IV, *ced-3(n717)*, *ced-5(n1812)*; LG V, *egl-1(n3082)*; and LG X, *ppk-3(n2668)*. The integrated arrays *bIs1* (P_{vit-2}VIT-2::GFP), *pwIs116* (P_{rme-2}RME-2::GFP), and *pwIs281* (P_{pie-1}GFP::CAV-1) were provided by B. Grant (Rutgers University, Piscataway, NJ). The integrated array *bpIs220* (P_{lgg-2}GFP::LGG-2) was provided by H. Zhang (Institute of Biophysics, Chinese Academy of Sciences, Beijing, China). *opIs334* (P_{ced-1}YFP::2xFYVE) was provided by K.S. Ravichandran (University of Virginia, Charlottesville, VA). The integrated arrays *smIs18* (HIS-24::GFP) and *smIs34* (P_{ced-1}CED-1::GFP) were provided by D. Xue (University of Colorado, Boulder, CO). The integrated array *ujIs113* (P_{pie-1}H2B::mCh + P_{nhr-2}HIS-24::mCh) was provided by Z. Du (Institute of Genetics and Developmental Biology, Chinese Academy of Sciences, Beijing, China). Other strains used in this study carrying integrated or extrachromosomal arrays were generated in the authors' laboratories and are as follows: *yqIs166* ($P_{slc-36.1}$GFP::SLC-36.1), *yqIs184* (P_{ced-1}mCh::SLC-36.1), *yqIs191* (P_{ced-1}GFP::PPK-3), *qxIs66* (P_{ced-1}GFP::RAB-7), *qxIs257* (P_{ced-1}NUC-1::mCh), *qxIs353* (P_{ced-1}LAAT-1::mCh), *qxIs354* (P_{ced-1}LAAT-1::GFP), *qxIs468* (P_{myo-3}LAAT-1::GFP), *yqEx1106*, *1107*, *1108* ($P_{slc-36.1}$SLC-36.1), *yqEx1109*, *1110*, *1111* ($P_{slc-36.1}$SLC-36.1(ΔiGsGif)), *yqEx1165*, *1166*, *1167* ($P_{slc-36.1}$SLC-36.1(H57A)), *yqEx1168*, *1169*, *1170* ($P_{slc-36.1}$SLC-36.1(P130L)), *yqEx1171*, *1172*, *1173* ($P_{slc-36.1}$SLC-36.1(G66A)), *yqEx1174*, *1175*, *1176* ($P_{slc-36.1}$SLC-36.1(L68S)), *yqEx1177*, *1178*, *1179* ($P_{slc-36.1}$SLC-36.1(S69A)), *yqEx1388*, *1389*, *1390* (P_{ced-1}mCh::SLC-36.1(H57A)), *yqEx1391*, *1392*, *1393* (P_{ced-1}mCh::SLC-36.1(G66A)), and *yqEx1394*, *1395*, *1396* (P_{ced-1}mCh::SLC-36.1(L68S)). The WormBase IDs of mutants and transgenic arrays are summarized in Table S1. The expressing vectors are listed in Table S2. Animals carrying the integrated arrays were outcrossed with the N2 strain four times. Deletion strains were outcrossed with the N2 strain at least four times. *C. elegans* cultures and genetic crosses were performed according to standard procedures.

Mutant isolation and cloning of *slc-36.1*, *ppk-3*, and *laat-1*

Synchronized L4-stage N2 animals were treated with 50 mM EMS for 4 h. The F2 embryos of EMS-treated animals were observed under differential interference contrast (DIC) microscopes. *yq24*, *51*, *80*, *84*, *90*, *93*, *95*, *110*, and *295* mutants were isolated based on the presence of embryonic vacuoles. *yq51* was mapped to the right end of LG III at the genetic map position +20.67(snp-WBVar00247063) by single nucleotide polymorphism mapping. Whole genome sequencing revealed a C to T mutation in exon 11 of *Y43F4B.7*, which results in substitution of Ser 336 with Phe. *yq80*, *84*, *90*, *93*, *95*, and *110* failed to complement with *yq51*, and mutations in *Y43F4B.7* were detected in these mutants. *yq84* and *yq93* mutants contained mutations in exons 4 and 12 of *Y43F4B.7*, resulting in substitutions of Pro 336 with Leu and Gly 394 with Gln, respectively. *yq110* mutants contained a point mutation (GA to AA) in the splicing acceptor site after exon 3, which leads to deletion of exon 3 (89 bp) in the transcript, resulting in an early stop codon in the encoded protein. *yq90*, *95*, and *80* mutants contained point mutations (AG to AA) in the splicing acceptor sites before exons 7, 10, and 12. These mutations led to deletion of exon 7 (98 bp), the first 32 bp of exon 10, and exon 12 (107 bp), respectively, resulting in early stop codons. Transformation rescuing experiments were performed by injecting a plasmid containing the *Y43F4B.7* ORF. All mutants were backcrossed with N2 animals at least four times.

yq24 mutants failed to complement *ppk-3(n2668)* mutants. The *yq24* mutation caused a S1448L mutation in the PPK-3 protein. *yq20*, *81*, and *295* mutants did not complement *laat-1(qx42)*. The *yq20*, *81*, and *295* mutations caused P266L, G270R, and C274Y, respectively, in the LAAT-1 protein.

Predication of topology and transmembrane regions

Topology models were exported from the Protter website. Transmembrane regions were predicted with the Phobius algorithm.

Generation of knock-in worms using CRISPR/Cas9

The insertion of tags at specific sites by CRISPR/Cas9 was performed as described before (Paix et al., 2014). Briefly, a single guide RNA (sgRNA) target site (5′-TCCTGATAGCCGTCTCTG GCAGG-3′) in the *slc-36.1* gene was used. The specific sgRNA target sequence was introduced into the vector pPD162-P_{eft-3} CAS9-P_{U6}sgRNA that expresses the Cas9 enzyme and sgRNA. GFP coding sequence with a 33-bp homologous arm containing four synonymous point mutations to prevent recutting was used as the homology-directed repair template. *dpy-10* was used as the positive selection marker as reported previously (Paix et al., 2014). Dumpy or roller F1 worms were examined for recombination by PCR. The recombinants were sequenced to confirm if homology-directed repair occurred correctly. The primers used are listed in Table S3.

Quantification of embryonic cell corpses and vacuoles

Embryos mounted on 2% agar pads were anesthetized in 3 µl M9 buffer (1 liter contains 3 g KH_2PO_4, 6 g Na_2HPO_4, 5 g NaCl, and 1 mM $MgSO_4$) containing 33 mM sodium azide. The numbers of button-like cell corpses and pit-like vacuoles in the head region

of living embryos at various developmental stages (comma, 1.5-fold, 2-fold, 2.5-fold, 3-fold, and 4-fold) were scored using DIC optics. 15 embryos at each developmental stage were scored for each strain. To examine embryonic cell corpse duration, embryos at the two-cell stage were mounted on 2% agar pads in egg salt buffer (118 mM NaCl and 48 mM KCl) at 20°C. Images in 30 Z-sections (1.0 µm/section) were captured every minute for 400 min using an Axioimager M2 microscope (ZEISS) equipped with an AxioCam monochrome digital camera (ZEISS). Images were processed and viewed using ZEN 2 pro software (ZEISS).

Quantification of phagosomal markers

WT and *slc-36.1(yq110)* embryos carrying CED-1::GFP, YFP::2xFYVE, GFP::RAB-7, LAAT-1::GFP, NUC-1::mCh, or CPL-1::mChiOnt transgene were mounted on 2% agar pads in egg salt buffer. Images of 1.5-fold stage embryos in 25 Z-sections (1.0 µm/section) were captured using an Axioimager M2 microscope (ZEISS). The percentage of button-like cell corpses labeled by phagosomal markers was determined by dividing the number of labeled cell corpses by the total number of button-like cell corpses. The percentage of vacuoles in *slc-36.1(yq110)* embryos labeled with phagosomal markers was determined by dividing the number of labeled vacuolar structures by the total number of vacuolar structures. 15 embryos were scored for each strain.

Examination of embryo hatching ratio

To examine embryonic development, 20 young adult worms (24 h after larval stage 4 [L4]) were placed on a fresh seeded nematode growth media (NGM) plate for 2 h. The worms were then removed, and the eggs laid on the plate were counted. Newly hatched L1 worms were counted until no new L1 worms hatched. More than 250 embryos were quantified for each strain. At least three independent experiments were performed.

Amino acid supplementation was performed by including free amino acids (Ameresco) at 100 mM in both NGM plates and OP50 culture spotted onto NGM plates. 10 *laat-1(yq295);slc-36.1(yq110)* L4 larvae were placed on the amino acid–supplemented plates and cultured for 7 d to yield adults. Then 30 adult animals were placed on the amino acid–supplemented plates for 2 h to produce eggs. The worms were then removed, and the hatch ratio of embryos was examined as described above. 10 independent experiments were performed.

Time-lapse imaging

Time-lapse imaging was performed at 20°C under a 100× 1.40-NA oil objective using the DeltaVision imaging system (DV Elite; GE Healthcare) coupled with a CoolSNAP camera (Photometric Scientifc) as described (Liu et al., 2016). Embryos (<50) were separated in 3 µl egg salt buffer and covered with a 2% agar pad in a glass-bottom dish (MatTek). The humidity in the dish was maintained with a piece of tissue paper saturated with water. Pre-comma embryos with 11 Z-section images (1.0 µm/section) were captured every 1 or 2 min for 120 min. Images were deconvoluted with the Enhanced Ratio option, and each Z-series was projected to form one image using the maximum-intensity projection option in softWoRx software coupled with DV Elite. Phagolysosome tubulation events and phagolysosome area were measured manually based on the projected image using softWoRx. 15 corpses were scored for each genotype. For more detailed monitoring, pre-comma embryos with 10 Z-section images (0.5 µm/section) were captured every 10 s for 20 min. To monitor ALR, adult worms (24 h after L4) were anesthetized in 3 µl M9 buffer containing 1 mM levamisole and covered with a 2% agar pad in a glass-bottom dish (MatTek). Posterior germline U-turn was marked. 10 Z-section images (0.35 µm/section) of the hypodermis in each genotype were captured every 5 s for 10 min. Images were deconvoluted and projected as above. The excitation filters used for GFP and mCh in all images were 488 and 559 nm, respectively.

Quantification of lysosomes in ABplaapppp cells

Embryos were separated in 3 µl egg salt buffer and covered with a 2% agar pad in a glass-bottom dish (MatTek). Comma-stage embryos were marked, and ABplaapppp cells containing LAAT-1::GFP–labeled phagolysosomes were captured with a Z-series of 0.2 µm/section for a total of 26 sections. LAAT-1::GFP–positive lysosome particles in ABplaapppp cells were counted. 40 or more embryos were analyzed for each genotype.

Quantification of hypodermal lysosome sizes

Adult worms (30 h after L4 or 24 h after L4 + 6 h starvation) were anesthetized in 3 µl M9 buffer containing 1 mM levamisole. Images of posterior hypodermis were captured. ZEN 2 pro software was used to automatically mark NUC-1::mCh–positive lysosomes and measure the area. Five worms were analyzed and >100 lysosomes were measured for each genotype.

MST protein–protein binding assay

MST was used to characterize protein interactions as described previously (Seidel et al., 2013; Asmari et al., 2018). Briefly, HEK293T cells were cultured at 37°C with 5% CO_2 in DMEM supplemented with 10% FBS (HyClone), 100 U/ml penicillin, and 100 mg/ml streptomycin. Transfections were performed with Lipofectamine 2000 (Invitrogen) according to the manufacturer's instructions. HEK293T cells overexpressing EGFP–SLC-36.1, EGFP, Myc–His–PPK-3, or Myc-His were lysed in 0.5 ml lysis buffer (10 mM Tris/Cl, pH 7.5, 150 mM NaCl; 0.5 mM EDTA; 0.5% NP-40, phosSTOP [Roche], and protease inhibitor cocktail [Roche]). Total protein concentrations of these cell lysates were measured with NanoDrop One (Thermo Fisher Scientific). Cell lysates were diluted with lysis buffer to a final concentration of 3.5 µg/µl. The fluorescent signals of the target proteins were examined, and no absorption, aggregation, or fluorescence variation was found. The signals of EGFP–SLC-36.1 and EGFP were well above the detection limit of the Monolith NT.115 instrument (NanoTemper Technologies). 10 µl of a mixture containing 7.5 µl ligand lysate and 2.5 µl target lysate expressing EGFP–SLC-36.1 or EGFP was loaded into NT.115 standard coated capillaries (NanoTemper Technologies). A series of cell lysates containing Myc–His–PPK-3 (0, 0.5, 1, 1.5, 2.0, 2.5, 3.0, 3.5, 4.0, 4.5, 5.0, 5.5, 6.0, 6.5, 7.0, and 7.5 µl) was used as ligands to build a ligand/target gradient. Lysates of Myc-His vector–expressing cells were used as a supplement to ensure

each reaction contained a similar amount of Myc-His proteins. MST measurements were performed at 25°C, 20% excitation power, and medium MST power. All experiments were repeated four times for each measurement. Data analyses were performed using NanoTemper analysis software.

Recombinant proteins and GST pull-down

Recombinant GST–SLC-36.1(1–53) and GST–SLC-36.1(101–142) proteins were expressed in Rosetta (DE3) bacterial cells and purified with glutathione-Sepharose beads (GE Healthcare) according to the instructions provided by the supplier. ^{35}S-labeled Myc–His–PPK-3(1–668) and Myc–His–PPK-3(669–1497) were prepared by in vitro translation using TNT T7-Coupled Reticulocyte Lysate System (Promega). Purified GST, GST–SLC-36.1(1–53), and GST–SLC-36.1(101–142) proteins (5 mg of each) immobilized on glutathione-Sepharose beads were preincubated with 2% BSA in binding buffer (50 mM Tris-HCl, pH 7.5, 100 mM NaCl, 0.1% NP-40, and 1 mM PMSF) for 1 h, and then incubated with ^{35}S-labeled Myc–His–PPK-3(1–668) and Myc–His–PPK-3(669–1497) in binding buffer containing 1% BSA at 4°C overnight. The resins were washed gently three times in washing buffer (20 mM Tris-HCl, pH 7.5, 50 mM NaCl, 0.1% NP-40, and PMSF). Bound proteins were resolved on SDS-PAGE and visualized by autoradiography.

RNAi

The bacteria feeding protocol was used in RNAi experiments. L4 larvae (P0) were cultured on the RNAi plates. The F1 progeny at the L4 stage were transferred to fresh RNAi plates and aged for 24 h. Adult F1 progeny were cultured for another 6 h on seeded or unseeded RNAi plates before the hypodermis was examined.

HVEM analysis

Adult worms (30 h after L4) were rapidly frozen using a high-pressure freezer (EM PACT2; Leica Biosystems). For embryos, 20 young adults (24 h after L4) were transferred to unseeded NGM plates. Worms were removed after 6 h, and embryos were harvested and rapidly frozen. Freeze substitution was performed in anhydrous acetone containing 1% osmium tetroxide. The samples were kept sequentially at −90°C for 72 h, −60°C for 8 h, and −30°C for 8 h and were finally brought to 20°C for 10 h in a freeze-substitution unit (EM AFS2; Leica Biosystems). The samples were washed three times (1 h each time) in fresh anhydrous acetone and were gradually infiltrated with Embed-812 resin in the following steps: resin/acetone 1:3 for 3 h, 1:1 for 5 h, 3:1 overnight, and 100% resin for 4 h. Samples were then kept overnight and embedded at 60°C for 48 h. The fixed samples were cut into 70-nm sections with a microtome EM UC7 (Leica Biosystems) and electron-stained with uranyl acetate and lead citrate. Sections were observed with a JEM-1400 (JEOL) operating at 80 kV.

Statistical analysis

Data were analyzed with Prism (GraphPad Software) or Excel (Microsoft Office) to generate curves or bar graphics. Error bars represent SEM. The two-tailed unpaired *t* test was used for statistical comparison of two groups of samples. One-way ANOVA followed by Dunnett's posttest was performed for statistical comparison of multiple groups of samples. *, $P < 0.05$; **, $P < 0.01$; ***, $P < 0.001$.

Online supplemental material

Fig. S1 analyzes SLC-36.1 expression pattern and subcellular localization in coelomocyte. Fig. S2 analyzes the dynamic change of HIS-24::GFP– and LAAT-1::mCh–positive phagolysosomes in N2 and *slc-36.1(yq110)* embryos, and lysosomal degradation of GFP::CAV-1, RME-2::GFP, and VIT-2::GFP in N2, *slc-36.1(lf)* and *laat-1(qx42)* embryos. Fig. S3 characterizes lysosome reformation from phagolysosomes in the N2 embryo. Fig. S4 shows that enlarged lysosomes in *slc-36.1(yq110)* hypodermis are positive for GFP::LGG-2 and NUC-1::mCh. Videos 1, 2, 3, 4, and 5 show time-lapse monitoring of phagolysosomal dynamics in N2, *slc-36.1(yq110)*, and *ppk-3(n2668)* embryos. Videos 6, 7, and 8 show time-lapse monitoring of lysosomal dynamics in N2, *slc-36.1(yq110)*, and *ppk-3(n2668)* adult hypodermis. Table S1 summarizes the WormBase IDs of mutants and transgenic arrays. Table S2 lists *C. elegans*, bacterial, and mammalian expression vectors. Table S3 lists primers used for GFP knock-in by CRISPR/Cas9.

Acknowledgments

We thank Drs. Hong Zhang and Shohei Mitani and the *C. elegans* genetic center for *C. elegans* strains and Dr. I. Hanson for proofreading the manuscript.

This research was supported by grants from the National Science Foundation of China (31730053) and the National Basic Research Program of China (2017YFA0503403).

The authors declare no competing financial interests.

Author contributions: Q. Gan and C. Yang conceived the study. Q. Gan did most of the experiments. X. Wang performed transmission EM analysis. Q. Zhang, Q. Yin, Y. Jian, Y. Liu, N. Xuan, J. Li, J. Zhou, K. Liu, Y. Jing, and X. Wang contributed to materials and experiments. Q. Gan and C. Yang wrote the manuscript with feedback from all authors.

Submitted: 15 January 2019
Revised: 29 April 2019
Accepted: 22 May 2019

References

Agulhon, C., P. Rostaing, P. Ravassard, C. Sagné, A. Triller, and B. Giros. 2003. Lysosomal amino acid transporter LYAAT-1 in the rat central nervous system: an in situ hybridization and immunohistochemical study. *J. Comp. Neurol.* 462:71–89. https://doi.org/10.1002/cne.10712

Alesutan, I.S., O.N. Ureche, J. Laufer, F. Klaus, A. Zürn, R. Lindner, N. Strutz-Seebohm, J.M. Tavaré, C. Boehmer, M. Palmada, et al. 2010. Regulation of the glutamate transporter EAAT4 by PIKfyve. *Cell. Physiol. Biochem.* 25:187–194. https://doi.org/10.1159/000276569

Asmari, M., R. Ratih, H.A. Alhazmi, and S. El Deeb. 2018. Thermophoresis for characterizing biomolecular interaction. *Methods.* 146:107–119. https://doi.org/10.1016/j.ymeth.2018.02.003

Audhya, A., I.X. McLeod, J.R. Yates, and K. Oegema. 2007. MVB-12, a fourth subunit of metazoan ESCRT-I, functions in receptor downregulation. *PLoS One.* 2:e956. https://doi.org/10.1371/journal.pone.0000956

Bissig, C., I. Hurbain, G. Raposo, and G. van Niel. 2017. PIKfyve activity regulates reformation of terminal storage lysosomes from endolysosomes. *Traffic.* 18:747–757. https://doi.org/10.1111/tra.12525

Bogatikov, E., C. Munoz, T. Pakladok, I. Alesutan, M. Shojaiefard, G. Seebohm, M. Föller, M. Palmada, C. Böhmer, S. Bröer, and F. Lang. 2012. Up-regulation of amino acid transporter SLC6A19 activity and surface protein abundance by PKB/Akt and PIKfyve. *Cell. Physiol. Biochem.* 30: 1538–1546. https://doi.org/10.1159/000343341

Bröer, S. 2014. The SLC38 family of sodium-amino acid co-transporters. *Pflugers Arch.* 466:155–172. https://doi.org/10.1007/s00424-013-1393-y

Chen, Y., and L. Yu. 2017. Recent progress in autophagic lysosome reformation. *Traffic.* 18:358–361. https://doi.org/10.1111/tra.12484

Chen, Y., and L. Yu. 2018. Development of Research into Autophagic Lysosome Reformation. *Mol. Cells.* 41:45–49.

Chen, D., H. Xiao, K. Zhang, B. Wang, Z. Gao, Y. Jian, X. Qi, J. Sun, L. Miao, and C. Yang. 2010. Retromer is required for apoptotic cell clearance by phagocytic receptor recycling. *Science.* 327:1261–1264. https://doi.org/10.1126/science.1184840

Conradt, B., and H.R. Horvitz. 1998. The C. elegans protein EGL-1 is required for programmed cell death and interacts with the Bcl-2-like protein CED-9. *Cell.* 93:519–529. https://doi.org/10.1016/S0092-8674(00)81182-4

Conradt, B., Y.C. Wu, and D. Xue. 2016. Programmed Cell Death During Caenorhabditis elegans Development. *Genetics.* 203:1533–1562. https://doi.org/10.1534/genetics.115.186247

Davidson, S.M., and M.G. Vander Heiden. 2017. Critical Functions of the Lysosome in Cancer Biology. *Annu. Rev. Pharmacol. Toxicol.* 57:481–507. https://doi.org/10.1146/annurev-pharmtox-010715-103101

Dong, X.P., D. Shen, X. Wang, T. Dawson, X. Li, Q. Zhang, X. Cheng, Y. Zhang, L.S. Weisman, M. Delling, and H. Xu. 2010. PI(3,5)P(2) controls membrane trafficking by direct activation of mucolipin Ca(2+) release channels in the endolysosome. *Nat. Commun.* 1:38. https://doi.org/10.1038/ncomms1037

Ellis, H.M., and H.R. Horvitz. 1986. Genetic control of programmed cell death in the nematode C. elegans. *Cell.* 44:817–829. https://doi.org/10.1016/0092-8674(86)90004-8

Ferguson, S.M. 2015. Beyond indigestion: emerging roles for lysosome-based signaling in human disease. *Curr. Opin. Cell Biol.* 35:59–68. https://doi.org/10.1016/j.ceb.2015.04.014

Flannagan, R.S., V. Jaumouillé, and S. Grinstein. 2012. The cell biology of phagocytosis. *Annu. Rev. Pathol.* 7:61–98. https://doi.org/10.1146/annurev-pathol-011811-132445

Gehring, E.M., A. Zurn, F. Klaus, J. Laufer, M. Sopjani, R. Lindner, N. Strutz-Seebohm, J.M. Tavaré, C. Boehmer, M. Palmada, et al. 2009. Regulation of the glutamate transporter EAAT2 by PIKfyve. *Cell. Physiol. Biochem.* 24:361–368. https://doi.org/10.1159/000257428

Grant, B., and D. Hirsh. 1999. Receptor-mediated endocytosis in the Caenorhabditis elegans oocyte. *Mol. Biol. Cell.* 10:4311–4326. https://doi.org/10.1091/mbc.10.12.4311

Gumienny, T.L., E. Lambie, E. Hartwieg, H.R. Horvitz, and M.O. Hengartner. 1999. Genetic control of programmed cell death in the Caenorhabditis elegans hermaphrodite germline. *Development.* 126:1011–1022.

Guo, P., T. Hu, J. Zhang, S. Jiang, and X. Wang. 2010. Sequential action of Caenorhabditis elegans Rab GTPases regulates phagolysosome formation during apoptotic cell degradation. *Proc. Natl. Acad. Sci. USA.* 107: 18016–18021. https://doi.org/10.1073/pnas.1008946107

Heublein, S., S. Kazi, M.H. Ogmundsdóttir, E.V. Attwood, S. Kala, C.A. Boyd, C. Wilson, and D.C. Goberdhan. 2010. Proton-assisted amino-acid transporters are conserved regulators of proliferation and amino-acid-dependent mTORC1 activation. *Oncogene.* 29:4068–4079. https://doi.org/10.1038/onc.2010.177

Horvitz, H.R. 2003. Worms, life, and death (Nobel lecture). *ChemBioChem.* 4: 697–711. https://doi.org/10.1002/cbic.200300614

Kinchen, J.M., and K.S. Ravichandran. 2008. Phagosome maturation: going through the acid test. *Nat. Rev. Mol. Cell Biol.* 9:781–795. https://doi.org/10.1038/nrm2515

Klaus, F., E.-M. Gehring, A. Zürn, J. Laufer, R. Lindner, N. Strutz-Seebohm, J.M. Tavaré, J.D. Rothstein, C. Boehmer, M. Palmada, et al. 2009. Regulation of the Na(+)-coupled glutamate transporter EAAT3 by PIKfyve. *Neurochem. Int.* 54:372–377. https://doi.org/10.1016/j.neuint.2009.01.002

Krajcovic, M., S. Krishna, L. Akkari, J.A. Joyce, and M. Overholtzer. 2013. mTOR regulates phagosome and entotic vacuole fission. *Mol. Biol. Cell.* 24:3736–3745. https://doi.org/10.1091/mbc.e13-07-0408

Krishna, S., W. Palm, Y. Lee, W. Yang, U. Bandyopadhyay, H. Xu, O. Florey, C.B. Thompson, and M. Overholtzer. 2016. PIKfyve Regulates Vacuole Maturation and Nutrient Recovery following Engulfment. *Dev. Cell.* 38: 536–547. https://doi.org/10.1016/j.devcel.2016.08.001

Li, W., W. Zou, D. Zhao, J. Yan, Z. Zhu, J. Lu, and X. Wang. 2009. C. elegans Rab GTPase activating protein TBC-2 promotes cell corpse degradation by regulating the small GTPase RAB-5. *Development.* 136:2445–2455. https://doi.org/10.1242/dev.035949

Li, Y., M. Xu, X. Ding, C. Yan, Z. Song, L. Chen, X. Huang, X. Wang, Y. Jian, G. Tang, et al. 2016. Protein kinase C controls lysosome biogenesis independently of mTORC1. *Nat. Cell Biol.* 18:1065–1077. https://doi.org/10.1038/ncb3407

Li, Z., N. Lu, X. He, and Z. Zhou. 2013. Monitoring the clearance of apoptotic and necrotic cells in the nematode Caenorhabditis elegans. *Methods Mol. Biol.* 1004:183–202. https://doi.org/10.1007/978-1-62703-383-1_14

Liu, B., H. Du, R. Rutkowski, A. Gartner, and X. Wang. 2012. LAAT-1 is the lysosomal lysine/arginine transporter that maintains amino acid homeostasis. *Science.* 337:351–354. https://doi.org/10.1126/science.1220281

Liu, K., Y. Jian, X. Sun, C. Yang, Z. Gao, Z. Zhang, X. Liu, Y. Li, J. Xu, Y. Jing, et al. 2016. Negative regulation of phosphatidylinositol 3-phosphate levels in early-to-late endosome conversion. *J. Cell Biol.* 212:181–198. https://doi.org/10.1083/jcb.201506081

Lu, Q., P. Yang, X. Huang, W. Hu, B. Guo, F. Wu, L. Lin, A.L. Kovács, L. Yu, and H. Zhang. 2011. The WD40 repeat PtdIns(3)P-binding protein EPG-6 regulates progression of omegasomes to autophagosomes. *Dev. Cell.* 21: 343–357. https://doi.org/10.1016/j.devcel.2011.06.024

Luzio, J.P., P.R. Pryor, and N.A. Bright. 2007. Lysosomes: fusion and function. *Nat. Rev. Mol. Cell Biol.* 8:622–632. https://doi.org/10.1038/nrm2217

Martina, J.A., H.I. Diab, L. Lishu, L. Jeong-A, S. Patange, N. Raben, and R. Puertollano. 2014. The nutrient-responsive transcription factor TFE3 promotes autophagy, lysosomal biogenesis, and clearance of cellular debris. *Sci. Signal.* 7:ra9. https://doi.org/10.1126/scisignal.2004754

McCartney, A.J., Y. Zhang, and L.S. Weisman. 2014. Phosphatidylinositol 3,5-bisphosphate: low abundance, high significance. *BioEssays.* 36:52–64. https://doi.org/10.1002/bies.201300012

Metzner, L., K. Natho, K. Zebisch, M. Dorn, E. Bosse-Doenecke, V. Ganapathy, and M. Brandsch. 2008. Mutational analysis of histidine residues in the human proton-coupled amino acid transporter PAT1. *Biochim. Biophys. Acta.* 1778:1042–1050. https://doi.org/10.1016/j.bbamem.2007.12.026

Miller, A., J. Schafer, C. Upchurch, E. Spooner, J. Huynh, S. Hernandez, B. McLaughlin, L. Oden, and H. Fares. 2015. Mucolipidosis type IV protein TRPML1-dependent lysosome formation. *Traffic.* 16:284–297. https://doi.org/10.1111/tra.12249

Nicot, A.S.2006. The Phosphoinositide Kinase PIKfyve/Fab1p Regulates Terminal Lysosome Maturation in Caenorhabditis elegans. *Mol. Biol. Cell.*17:3062–3074.

Paix, A., Y. Wang, H.E. Smith, C.Y. Lee, D. Calidas, T. Lu, J. Smith, H. Schmidt, M.W. Krause, and G. Seydoux. 2014. Scalable and versatile genome editing using linear DNAs with microhomology to Cas9 Sites in Caenorhabditis elegans. *Genetics.* 198:1347–1356. https://doi.org/10.1534/genetics.114.170423

Perera, R.M., and R. Zoncu. 2016. The Lysosome as a Regulatory Hub. *Annu. Rev. Cell Dev. Biol.* 32:223–253. https://doi.org/10.1146/annurev-cellbio-111315-125125

Pryor, P.R., B.M. Mullock, N.A. Bright, S.R. Gray, and J.P. Luzio. 2000. The role of intraorganellar Ca(2+) in late endosome-lysosome heterotypic fusion and in the reformation of lysosomes from hybrid organelles. *J. Cell Biol.* 149:1053–1062. https://doi.org/10.1083/jcb.149.5.1053

Puertollano, R., S.M. Ferguson, J. Brugarolas, and A. Ballabio. 2018. The complex relationship between TFEB transcription factor phosphorylation and subcellular localization. *EMBO J.* 37:e98804. https://doi.org/10.15252/embj.201798804

Reddien, P.W., and H.R. Horvitz. 2004. The engulfment process of programmed cell death in caenorhabditis elegans. *Annu. Rev. Cell Dev. Biol.* 20:193–221. https://doi.org/10.1146/annurev.cellbio.20.022003.114619

Rong, Y., C.K. McPhee, S. Deng, L. Huang, L. Chen, M. Liu, K. Tracy, E.H. Baehrecke, L. Yu, and M.J. Lenardo. 2011. Spinster is required for autophagic lysosome reformation and mTOR reactivation following starvation. *Proc. Natl. Acad. Sci. USA.* 108:7826–7831. https://doi.org/10.1073/pnas.1013800108

Saftig, P., and J. Klumperman. 2009. Lysosome biogenesis and lysosomal membrane proteins: trafficking meets function. *Nat. Rev. Mol. Cell Biol.* 10:623–635. https://doi.org/10.1038/nrm2745

Sagné, C., C. Agulhon, P. Ravassard, M. Darmon, M. Hamon, S. El Mestikawy, B. Gasnier, and B. Giros. 2001. Identification and characterization of a lysosomal transporter for small neutral amino acids. *Proc. Natl. Acad. Sci. USA.* 98:7206–7211. https://doi.org/10.1073/pnas.121183498

Sasaki, A., I. Nakae, M. Nagasawa, K. Hashimoto, F. Abe, K. Saito, M. Fukuyama, K. Gengyo-Ando, S. Mitani, T. Katada, and K. Kontani. 2013.

Arl8/ARL-8 functions in apoptotic cell removal by mediating phagolysosome formation in Caenorhabditis elegans. *Mol. Biol. Cell.* 24: 1584–1592. https://doi.org/10.1091/mbc.e12-08-0628

Sato, K., M. Sato, A. Audhya, K. Oegema, P. Schweinsberg, and B.D. Grant. 2006. Dynamic regulation of caveolin-1 trafficking in the germ line and embryo of Caenorhabditis elegans. *Mol. Biol. Cell.* 17:3085–3094. https://doi.org/10.1091/mbc.e06-03-0211

Seidel, S.A., P.M. Dijkman, W.A. Lea, G. van den Bogaart, M. Jerabek-Willemsen, A. Lazic, J.S. Joseph, P. Srinivasan, P. Baaske, A. Simeonov, et al. 2013. Microscale thermophoresis quantifies biomolecular interactions under previously challenging conditions. *Methods.* 59:301–315. https://doi.org/10.1016/j.ymeth.2012.12.005

Settembre, C., C. Di Malta, V.A. Polito, M. Garcia Arencibia, F. Vetrini, S. Erdin, S.U. Erdin, T. Huynh, D. Medina, P. Colella, et al. 2011. TFEB links autophagy to lysosomal biogenesis. *Science.* 332:1429–1433. https://doi.org/10.1126/science.1204592

Settembre, C., A. Fraldi, D.L. Medina, and A. Ballabio. 2013. Signals from the lysosome: a control centre for cellular clearance and energy metabolism. *Nat. Rev. Mol. Cell Biol.* 14:283–296. https://doi.org/10.1038/nrm3565

Shang, P., M. Valapala, R. Grebe, S. Hose, S. Ghosh, I.A. Bhutto, J.T. Handa, G.A. Lutty, L. Lu, J. Wan, et al. 2017. The amino acid transporter SLC36A4 regulates the amino acid pool in retinal pigmented epithelial cells and mediates the mechanistic target of rapamycin, complex 1 signaling. *Aging Cell.* 16:349–359. https://doi.org/10.1111/acel.12561

Shojaiefard, M., N. Strutz-Seebohm, J.M. Tavaré, G. Seebohm, and F. Lang. 2007. Regulation of the Na(+), glucose cotransporter by PIKfyve and the serum and glucocorticoid inducible kinase SGK1. *Biochem. Biophys. Res. Commun.* 359:843–847. https://doi.org/10.1016/j.bbrc.2007.05.111

Sopjani, M., A. Kunert, K. Czarkowski, F. Klaus, J. Laufer, M. Föller, and F. Lang. 2010. Regulation of the Ca(2+) channel TRPV6 by the kinases SGK1, PKB/Akt, and PIKfyve. *J. Membr. Biol.* 233:35–41. https://doi.org/10.1007/s00232-009-9222-0

Sulston, J.E., and H.R. Horvitz. 1977. Post-embryonic cell lineages of the nematode, Caenorhabditis elegans. *Dev. Biol.* 56:110–156. https://doi.org/10.1016/0012-1606(77)90158-0

Sulston, J.E., E. Schierenberg, J.G. White, and J.N. Thomson. 1983. The embryonic cell lineage of the nematode Caenorhabditis elegans. *Dev. Biol.* 100:64–119. https://doi.org/10.1016/0012-1606(83)90201-4

Wang, X., and C. Yang. 2016. Programmed cell death and clearance of cell corpses in Caenorhabditis elegans. *Cell. Mol. Life Sci.* 73:2221–2236. https://doi.org/10.1007/s00018-016-2196-z

Xiao, H., D. Chen, Z. Fang, J. Xu, X. Sun, S. Song, J. Liu, and C. Yang. 2009. Lysosome biogenesis mediated by vps-18 affects apoptotic cell degradation in Caenorhabditis elegans. *Mol. Biol. Cell.* 20:21–32. https://doi.org/10.1091/mbc.e08-04-0441

Xu, H., and D. Ren. 2015. Lysosomal physiology. *Annu. Rev. Physiol.* 77:57–80. https://doi.org/10.1146/annurev-physiol-021014-071649

Xu, M., Y. Liu, L. Zhao, Q. Gan, X. Wang, and C. Yang. 2014. The lysosomal cathepsin protease CPL-1 plays a leading role in phagosomal degradation of apoptotic cells in Caenorhabditis elegans. *Mol. Biol. Cell.* 25: 2071–2083. https://doi.org/10.1091/mbc.e14-01-0015

Zheng, L., W. Zhang, Y. Zhou, F. Li, H. Wei, and J. Peng. 2016. Recent Advances in Understanding Amino Acid Sensing Mechanisms that Regulate mTORC1. *Int. J. Mol. Sci.* 17:E1636. https://doi.org/10.3390/ijms17101636